NUMERICAL AND EXPERIMENTAL STUDY OF DELAMINATION IN LAMINATED COMPOSITES

by

Ender Alper TOP

Submitted to the Institute of Graduate Studies in
Science and Engineering in partial fulfillment of
the requirements for the degree of
Master of Science
in
Mechanical Engineering

Yeditepe University

2010

NUMERICAL AND EXPERIMENTAL STUDY OF DELAMINATION IN LAMINATED COMPOSITES

APPROVED BY:

Prof. Dr Mehmet A. AKGÜN
(Thesis Supervisor) .....

Assoc. Prof. Erol ŞENOCAK .....

Asst. Prof. A. Fethi OKYAR .....

Asst. Prof. Namık ÇIBLAK .....

DATE OF APPROVAL: / /

ACKNOWLEDGEMENTS

I would like to thank my advisor Prof. Dr. Mehmet A. AKGÜN for his guidance and support throughout this study.

I also thank Asst. Prof. Dr. Dilek TURAN and Research Assistant Ramazan KALE for conducting the fatigue tests in Eskişehir Anadolu University.

Special thanks are due TAI (Turkish Aerospace Industry) for manufacturing all of the test specimens used in the study. Without their help this thesis could not be completed. Finally, I would like to thank my family and my friends for their encouragement.

ABSTRACT

NUMERICAL AND EXPERIMENTAL STUDY OF DELAMINATION IN LAMINATED COMPOSITES

In this study, delamination growth in a double cantilever beam (DCB) specimen, which is used to measure critical strain energy release rate under a mode I type of loading, was investigated experimentally and numerically. In addition, delamination growth in mixed mode beam (MMB) specimens was tested to measure critical strain energy release rates under mixed mode I and mode II types of loading and fatigue tests were conducted on tapered laminates.

The material in all cases was carbon fiber reinforced epoxy. The laminates were manufactured from UD (Unidirectional) carbon tapes. Delamination growth was simulated with a fracture mechanics approach, virtual crack closure technique (VCCT), using the finite element method. In order to implement the VCCT method element–killing strategy was used. This provided a means to handle moving meshes during delamination propagation. Simple tension tests and three point bending tests were conducted as well to determine basic material properties.

ÖZET

TABAKALI KOMPOZİTLERDE KATMANLAR ARASI AYRIŞMANIN SAYISAL VE DENEYSEL İNCELENMESİ

Bu çalışmada, mod 1 tipi yük uygulaması altında gerinim enerjisi boşalmasının kritik değerinin ölçümünde kullanılan çifte ankastre kiriş nümunesinde katmanlar arası ayrışma büyümesi deneysel ve sayısal olarak incelenmiştir. Buna ek olarak, karışık olarak uygulanan mod 1 ve mod 2 tipi yükleri altında gerinim enerjisi boşalmasının kritik değerinin ölçmek amacıyla karışık mode kiriş nümuneleri test edildi. Ayrıca kat düşümlü değişken kesitli tabakalı kompozit plakalara yorulma testleri uygulandı.

Tüm nümuneler epoksi ile ön ıslatımlı tek yönlü karbon elyaf şeritten imal edilmiştir. Katmanlar arası ayrışma, bir kırılma mekaniği yaklaşımı olan, gerçek olmayan çatlak kapanma tekniği uygulamasıyla sonlu elemanlar metodu kullanılarak modellenmiştir. Bu metodun uygulanmasında eleman öldürme stratejisi kullanılmıştır. Bu strateji vasıtasıyla, ayrışma ilerlemesi sürecinde eleman ağının yer değiştirmesi temsil edilmiştir. Ayrıca malzeme özelliklerini belirlemek amacıyla temel çekme deneyi ve üç nokta bükme deneyleri yapılmıştır.

TABLE OF CONTENTS

LIST OF FIGURES

LIST OF TABLES

LIST OF SYMBOLS/ABBREVIATIONS

ΔG	Energy release rate range
a	Crack length
APDL	Ansys parametric design language
ASTM	American Society for Testing And Materials
b	width
c	Distance between roller and hinge holder
C, r	The constants for the propagation parameters in Paris-law
C/PEEK	Carbon-fiber-reinforced polyetheretherketone
CZM	Cohesive zone model
d	Distance
da/dN	Propagation rate of delamination
DCB	Double cantilever beam
E_{11}, E_{22}, E_{33}	Elasticity moduli along material directions
E_f	Flexural modulus
ELS	End-loaded split
ENF	End-Notched Flexure
F	Force
$F_{cd}^{y}, F_{cd}^{x}\ and\ F_{cd}^{z}$	In Figure 2.9, the magnitudes of nodal force pairs at nodes c and d in the y, x and z directions, respectively
FEM	Finite element method
G_1, G_2, G_3	Strain energy release rate in x, y, z directions respectively
G_c	Critical strain energy release rate
$G_{Ic}, G_{IIc}, G_{IIIc}$	Critical strain energy release rate along material direction 1 2 and 3
G_{th}	Threshold energy release rate
h	Half thickness of the DCB
IMES	Istanbul Metallic Manufacturers Complex
L	Length
m	Slope of the fitting line of the flexural modulus

m,n	Material parameters
MMB	Mixed mode beam
MPC	Multi point constraint
N	Number of cycles
P	Reaction force
Pmax	Maximum force applied
R	Reversion index
S	Span
t	thickness
u, v, w	Displacement components in x, y, z directions, respectively
UD	Unidirectional
VCCT	Virtual crack closure technique
W	Work (by means of energy)
δ	Tip-load displacement of MMB and DCB specimens
ν_{12} ν_{13} ν_{23}	Poisons ratios along material directions

INTRODUCTION

Use of polymer matrix composite materials with continuous fibers has gained popularity (despite their generally high cost) in the area of structural applications. It is a result of the unique mechanical properties of these materials (e.g., excellent stiffness/weight and strength/weight ratios, easy formability, and corrosion resistance). They are appropriate for high-performance products that need to be lightweight, and strong enough to take harsh loading conditions. Therefore, they are most widely used in aerospace industry. They are used in other sectors such as in naval engineering, civil engineering, automobile industry and sporting equipment.

The most important failure mode for composites is delamination. This mode of damage is essentially three-dimensional in nature, and interlaminar stresses are primarily responsible for it [1]. Delamination growth may be due to an increase of the static load being applied or due to repetitive loading, as in fatigue-driven delamination. Delamination may occur under Mode 1 (opening mode), Mode 2 (in-plane shear) and\or Mode 3 (tearing mode) type of loading. A combination of these modes may be present, which makes testing difficult.

Since delamination can cause a composite structure to fail, there is a need to study delamination. Utilization of composite materials requires knowledge of how delamination failure can be prevented, so that a good design of a desired component can be achieved. In addition, if there is fatigue loading, a better design requires “fatigue durability”. This phenomenon is still hard to handle due to the complexity of the composite materials.

In order to achieve a better design experiments or computer simulations can be carried out. However, experimentation tends to be a lengthy and expensive process and so in recent years a lot of emphasis has been placed on computer simulations.

Composites plates are tapered in thickness for weight saving. Tapering is achieved over a short distance which causes stress concentrations. In addition, there are transverse stresses which may lead to delamination. Modeling of delamination in a tapered laminate

under fatigue loading is a challenging task. This thesis work began as an attempt at this task. The objective was to test and simulate the behavior of tapered laminated carbon coupons under fatigue loading. The experimental work involved standard static materials testing and fracture toughness testing as well. However, because of experimental difficulties, fatigue tests did not proceed as expected.

The thesis work now involves tests for fracture toughness measurement as well as simulation of the testing process. Pure mode 1 and combined mode 1 and mode 2 delamination tests are carried with proper fixtures. The delamination process in DCB specimens is modeled and analyzed with the finite element method. The theoretical and experimental results are compared in the text. The result of the fatigue tests are also be reported and commented on.

THEORY, STATE OF THE ART AND LITERATURE SURVEY

1.1. CAUSES OF DELAMINATION

Causes of delamination can be grouped in two categories [2,3]. One of these categories is delamination due to curvature as in curved segments, tubular sections, cylinders and spheres, and pressurized containers. In such delaminations, normal and shear stresses at the interface of two adjacent plies can lead to loss of adhesion and initiation of an interlaminar crack.

The other category includes abrupt changes in sections, such as ply drop-offs, couplings between stiffeners and thin plates, free edges and bonded and bolted joints. A third category related with temperature and moisture effects can be added. During the curing process of a laminate, the difference between the thermal coefficients of matrix and reinforcement results in differential contractions between the plies. The residual stresses due to these phenomena might be a source of delamination [3,4]. Similarly, the differential expansion of the plies of a laminate during moisture absorption might be a cause for delamination [3,5].

One other reason for delamination is the formation of resin rich pockets that result from poor practices when laying up the plies at the manufacturing stage [6,7]. Another reason arises in the case of transverse concentrated loads caused by low velocity impacts. Impact is an important source of delamination in composite structures. Interlaminar cracks can originate from internal damage in the interface between adjacent plies as a consequence of impact, from the drop of a tool during production, mounting or repairing, or from ballistic impacts in military planes or structures [7].

1.2. DELAMINATION TYPES

Types of delaminations are internal and near-surface delaminations [6,7]. An internal delamination originates in the inner ply interfaces of a laminate and can be due to the interaction of matrix cracks and ply interfaces. Delaminations originated by transverse

matrix cracks in plies orthogonal to the tensile load are common examples of this type of delamination.

Internal delamination reduces considerably the load-capacity of composite structures. In particular, when compression loads are applied, the overall flexural behavior of the laminate is significantly affected as shown schematically in Figure 2.1. Although delamination separates the laminate in two parts, there is an interaction between the deformation of one part of the laminate and the other. Due to this interaction, both parts of the laminate may deflect in a similar way.

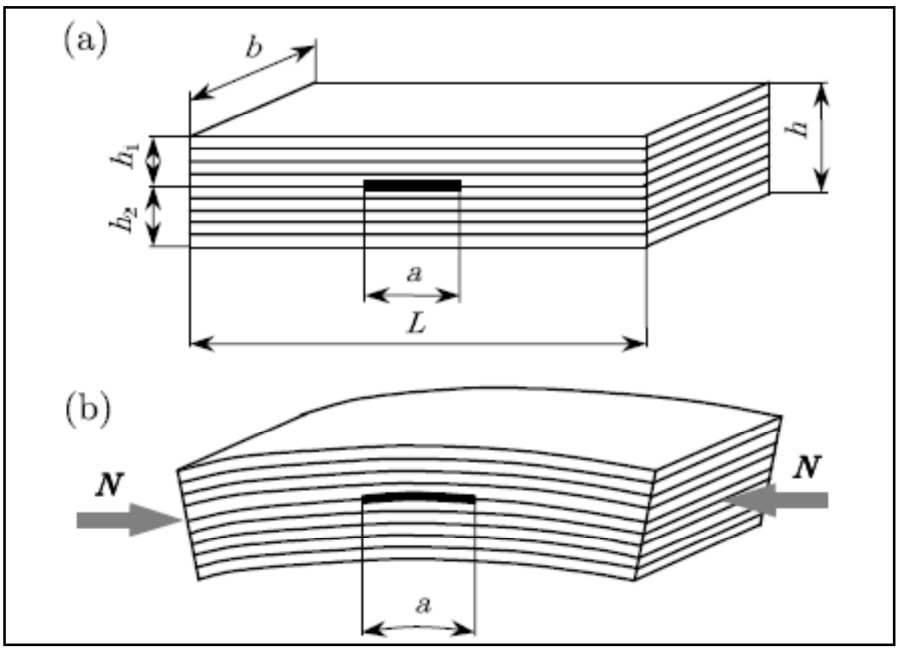

Figure 2.1. Internal delamination: a. disposition across the laminate and (b) effect on the overall stability [6]

Near-surface delaminations, as the name indicates, originate near the surface of a laminate and represent a more complex scenario than internal delaminations. The deformation of the delaminated part is less influenced by the deformation of the rest of the laminate. Therefore, the deformation of a near-surface delaminated part does not necessarily follow the deformation of the rest of the laminate. Consequently, not only the growth of the near-surface delamination has to be taken into account but also its local stability. Bolotin [6,7] classified different types of near-surface delaminations that

can originate in a composite plate component in different load conditions as shown in Figure 2.2.

After initiation, internal or near-surface delaminations can propagate under either static or fatigue loads. In both cases, the reduction in strength and stability of a composite part is considerable.

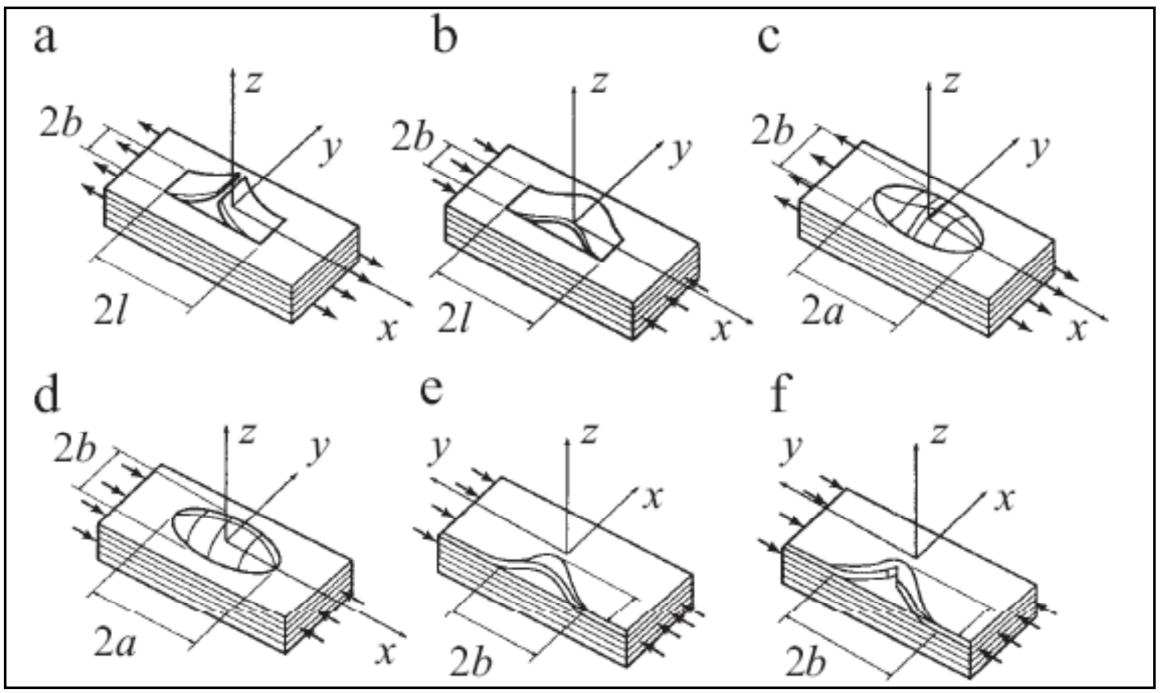

Figure 2.2. Near-surface delamination: a. open in tension; b. closed in compression; c. open buckled; d. closed buckled; e. edge buckled and f. edge buckled with secondary crack [6]

1.3. MICROMECHANISM OF DELAMINATIONS

The growth of an interlaminar crack is preceded by the formation of a damage zone in the vicinity of the crack tip as illustrated in Figure 2.3. Depending on both the “resin toughness” and “the state of stress” the characterization of the deformation/damage zone is quite variable.

During delamination different fracture modes can be present. These failure modes can be classified as mode I (opening component), mode II (shear component perpendicular to the delamination front) and mode III (shear component parallel to the delamination front). These modes are shown in Figure 2.4

Under working conditions composites may not experience a single fracture mode but a combination of them. When more than one mode of fracture is present this is known as mixed-mode or mode mixity. This generates a delamination failure locus, toughness versus mode mixity. Figure 2.5 demonstrates “The Delamination Failure Locus for Hexcel T800/924” (a carbon fibre/modified epoxy). This locus is modeled to produce a delamination failure criterion [8,9]. There are many proposed failure criteria, ranging from those with an empirical basis [8,9] to some which have considered physical failure mechanisms, such as those proposed by Johanesson et al. [9,10] and Kinloch et al.[9,11].

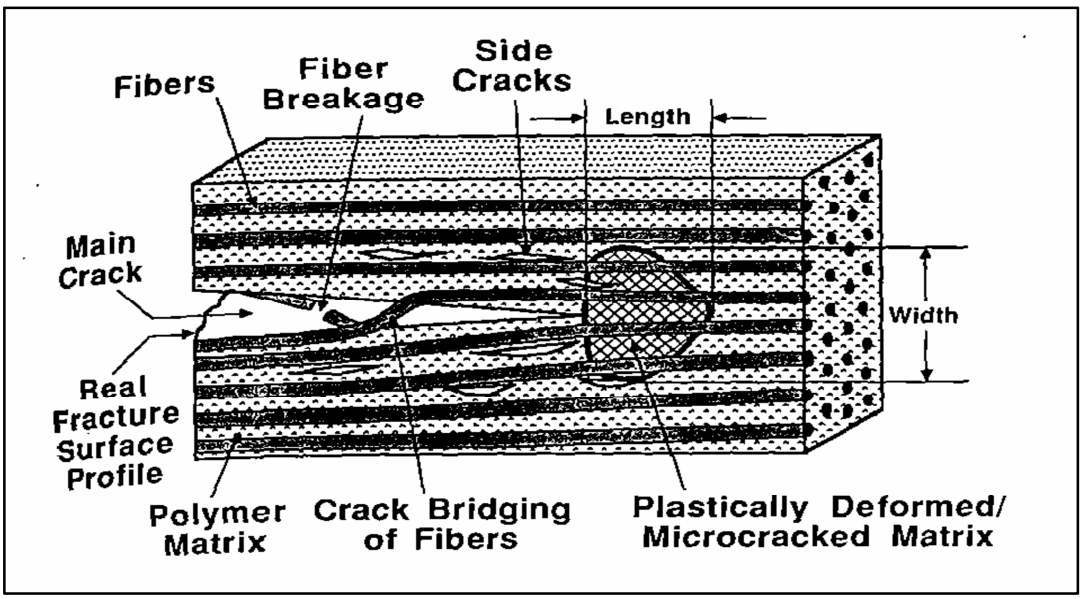

Figure 2.3. Damage zone in the vicinity of a crack tip [10]

In the vicinity of the crack tip for mode II or mode III loading, damage zone is greater than for mode I loading. A much slower decaying of the stress field ahead of the crack tip for the shear modes of loading is responsible for this difference [3].Sometimes, crack advance occurs by fiber-matrix debonding before microcrack coalescence occurs. When debonding takes place, fiber bridging and fiber breakage are observed. For ductile

systems, plastic deformation around the crack tip precedes crack advance. Crack advance generally occurs by ductile tearing, but crack advance by interfacial debonding was also commonly observed in composites made with more ductile resins [3,12].

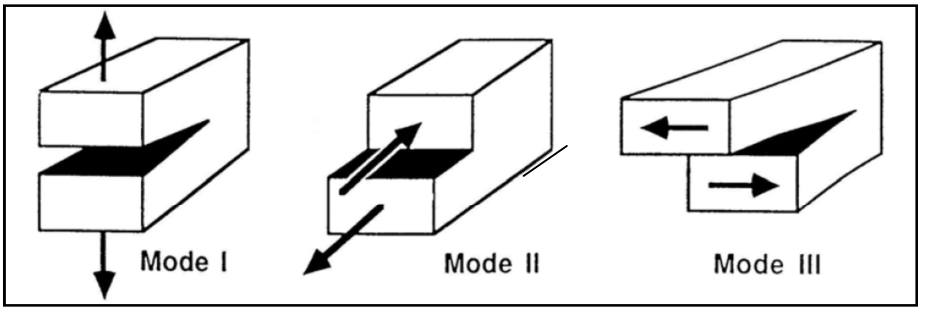

Figure 2.4. Mode I, mode II, and mode III crack propagation modes

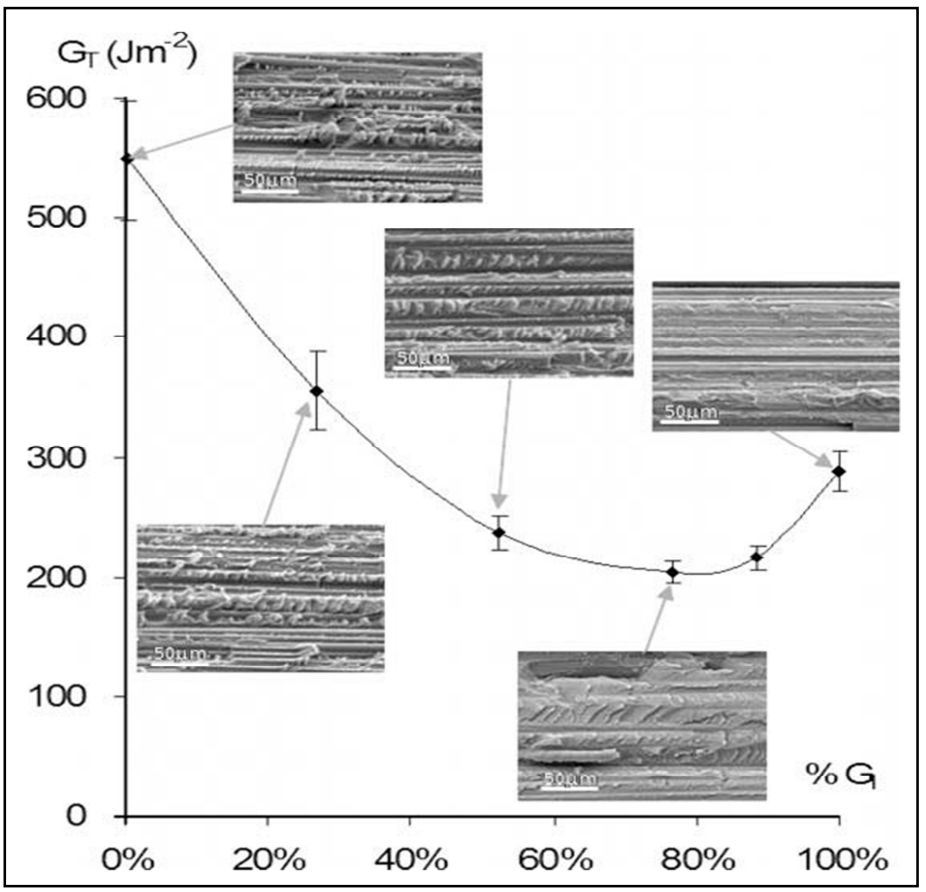

Figure 2.5. Toughness versus mode mixity % G for T800/94 showing the change in fracture morphology [9]

Shear mode delamination (mode II and/or mode III) of quasi-brittle systems occurs in a very distinctive way. Microcracks form from a considerable distance ahead of the crack tip, at a angle to the plane of the ply. These cracks grow until they reach the fibres, which bound the resin-rich region between plies. It sometimes appears that the cracks stop in the resin short of the nearest visible fiber. However there are certainly fibers just at the top or beneath the surface that are responsible for arresting these growing microcracks. Coalescence of these microcracks is required for macrocrack advance. This coalescence generally occurs at the fiber/matrix interface, giving a “corrugated roof appearance” along with the formation of “hackles” in the resin between fibers as in Figure 2.6. The fracture process for mode II delamination appears to be ductile rupture, with occasional fibre debonding [13].

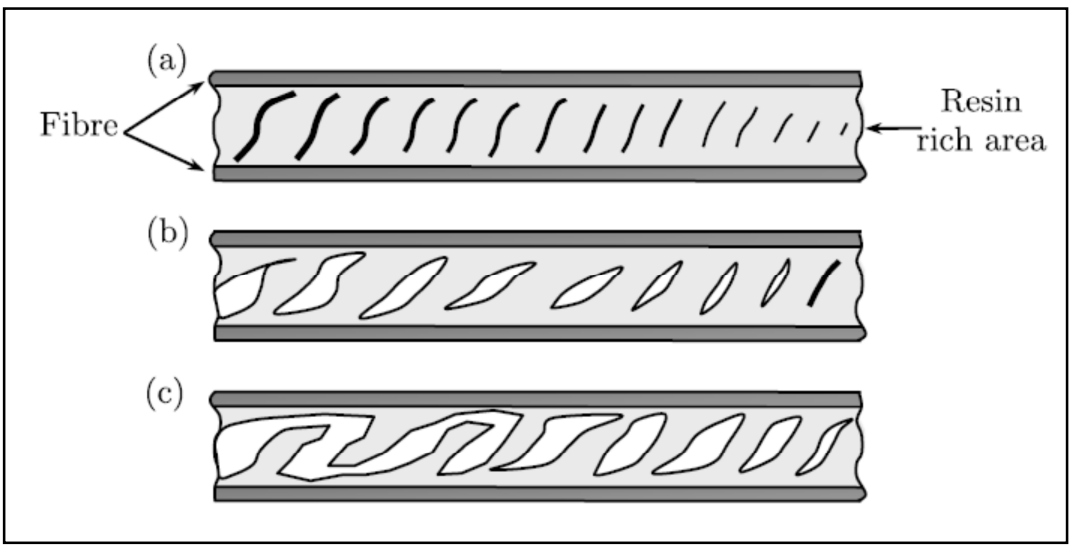

Figure 2.6. Formation and growth of a mode II delamination at the ply interface: a. microcrack formation ahead of the crack tip; b. microcrack growth and opening and c. microcrack coalescence accompanied by shear cusps [13]

1.4. EARLY STUDIES IN DELAMINATION MECHANICS

Historically, the delamination mechanics was first studied by Obreimoff (1894-1981), a Soviet expert in the field of solid-state physics. In 1930, he published in an English journal a paper under the title “The Splitting Strength of Mica” [6,14]. Obreimoff estimated the specific work of interlaminar fracture, examining the detaching

of a layer from a mica specimen under the action of a tearing force. The paper followed the series of pioneering papers in fracture mechanics by Griffith in 1920. The development of production engineering of composites and composite structures has aroused an interest in the delamination mechanics [6]. Among the studies in this line, the most famous paper belongs to Kachanov. In 1975, he stated and partially solved the problem on the stability of a thin internal delamination in a ring or a circular cylindrical shell of a layered composite under external hydrostatic compression.

From the early 1980's and up to the present day, the delamination mechanics has been a subject of ever-increasing interest. The number of studies in this field runs into thousands .

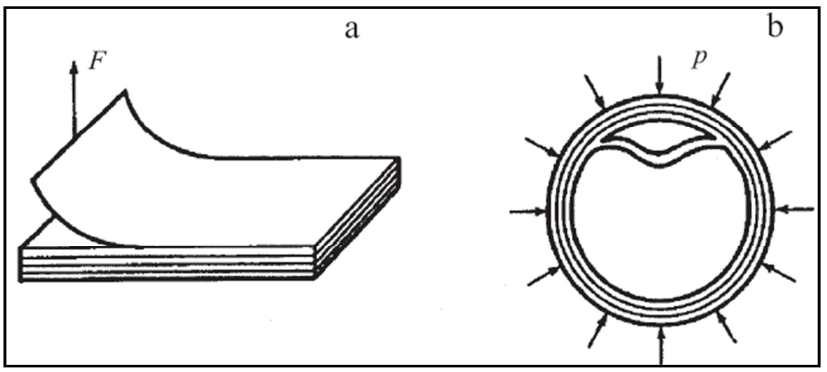

Figure 2.7. Pioneering Studies in delamination mechanics: Obreimoff (a) and Kachanov (b) problems [6]

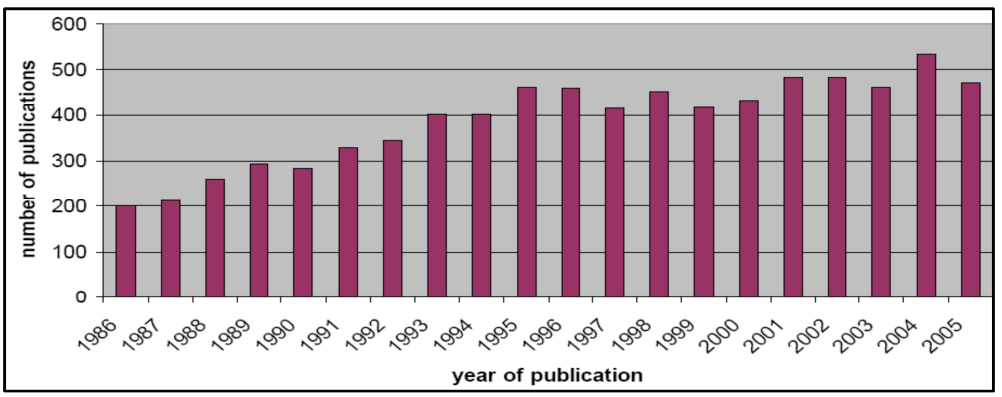

Figure 2.8. The number of publications per year about composites in the last twenty years (1986-2005) [15]

1.5. INTRODUCTION TO ENERGY APPROACH IN FRACTURE MECHANICS

The fracture of materials is a widely known problem and a lot of research and improvements have been achieved in this field. Fracture mechanics provides a tool for assessing the severity of flaws in structures. Linear elastic fracture mechanics (LEFM) is the basic theory of fracture, founded by Griffith (1920) [16,17]. He produced a theory based on a simple energy balance and concluded by Irwin (1957) [17,18], Rice (1968a, 1968b) [17, 19, 20], and Riveros (2006)[17,21]. The LEFM is a highly simplified theory which applies to any material under a basic ideal situation, where all the material is elastic except in the crack tip (Bazant and Planas 1998) [17,22].

Griffith's model worked fairly well with glass specimens however it did not work well with metals. However his approach formed a basis for every kind of fracture according to material which is fractured. This approach states stress at fracture as,

$$\sigma_f = \left(\frac{2Ew_f}{\pi a}\right)^{1/2} \tag{2.1}$$

where E is the total energy and w_f is the fracture energy which include plastic, viscoelastic, or viscoplastic effects depending on the material, a is the crack length which is opened, σ_f stress at fracture. Hence Irwin could have extended Griffith's theory to materials that have localized plastic deformation at the tip of the crack.

Irwin's approach is more suitable for solving engineering problems. Irwin defined an energy release rate, G, which is a measure of the energy available for an increment of crack extension. The term 'rate', as used in this context, does not refer to a derivative with respect to time. The energy release rate is the rate of change in potential energy with respect to the area swept through by the crack front [23].

1.6. VIRTUAL CRACK CLOSURE TECHNIQUE (VCCT)

The virtual crack closure technique is one of the most widely used procedures to predict crack propagation. This technique is based on Irwin's assumption that when a crack

extends by a small amount, the energy released in the process is equal to the work required to close the crack to its original length. If the energy released per unit area is greater than or equal to the critical value, G_c, the crack will propagate. The mode I, mode II and mode III energy release rates, and , respectively, can be computed from the nodal forces and displacements obtained from the solution of a finite element model [24,25].

In a finite element model such as shown in Figure 2.9, the energy released is the work done by the nodal forces required to close the crack tip. Thus:

—— (2.2)

—— (2.3)

—— (2.4)

where b is the specimen thickness are the magnitudes of nodal force pairs at nodes c and d in the y, x and z directions, respectively. and are the nodal displacements before nodes c and d are pulled together, is the crack length increment.

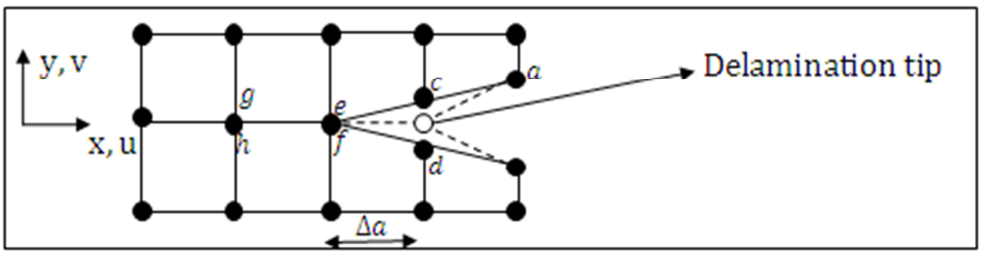

Figure 2.9. Calculation of the energy release rate using Virtual Crack Closure Technique

The analysis can be done in two steps, using the first step to compute the values of the nodal forces required to hold the nodes c and d together, and the

relative displacement components between nodes c and d are calculated in the second step. However, the analysis can be simplified by replacing the corresponding components of nodal forces by F_{ef}^{y}, F_{ef}^{x} and F_{ef}^{z} (Rybicki and Kanninen [25, 26]).

After the above steps, G_I, G_{II} and G_{III} are calculated and the summation of these three strain energy release rates gives the total strain energy release rate as shown below.

$$G_T = G_I + G_{II} + G_{III} \tag{2.5}$$

Crack propagation is formed when the total energy release rate is equal to the critical fracture toughness of the material, G_c:

$$G_T = G_c \tag{2.6}$$

One of the benefits of this form of calculation is that it is based on energy rather than stress. The main disadvantage of the VCCT technique is that it is based on the assumption of self-similar propagation, i.e., the forces F_{ef}^{i} and F_{cd}^{i} are the same. Thus, crack initiation and the propagation of short cracks cannot be predicted. Only crack propagation could be predicted, regardless of crack initiation.

1.7. COHESIVE ZONE MODEL

The view from which cohesive zone models originate suggests fracture as a gradual occurrence in which separation takes place along an extended crack 'tip', or cohesive zone and is resisted by cohesive tractions (Ortiz and Pandolfi, 1999) [27]. Therefore, cohesive zone elements for the implementation of cohesive zone models do not represent any physical material, but describe the cohesive forces which occur when material elements (such as grains) are being pulled apart. Thus, cohesive zone elements are placed between continuum (bulk) elements, as shown in Figure 2.10.

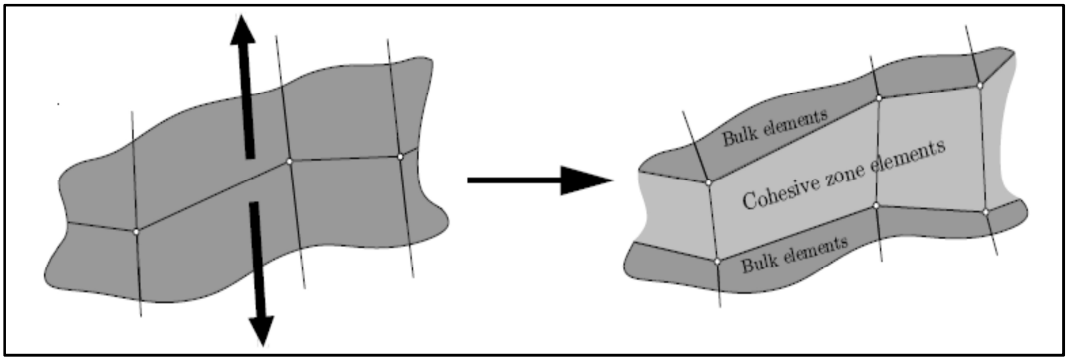

Figure 2.10. Application of cohesive zone elements along bulk element boundaries [28]

When damage growth occurs these cohesive zone elements open in order to simulate crack initiation or crack growth. Since the crack path can only follow these elements, the direction of crack propagation strongly depends on the presence or absence of cohesive zone elements, implying the crack path is mesh-dependent. However, refining the mesh reduces this problem. In two dimensions, tractions can occur in the normal and the shear direction. The description of the failure behavior is defined by traction-separation laws. These relations describe the tractions as a function of separations and determine the constitutive behavior of cohesive zone models is demonstrated in Figure 2.11. According to Chandra et al. (2002) there is a wide range in traction separation laws [29]; however, they all possess the same global behavior. As the cohesive surfaces separate, the traction first increases until a maximum is reached, and consequently the traction decreases to zero, which results in total (local) separation. When the area under the traction-displacement jump relation is equal to the fracture toughness G_c, the traction is decreased to zero and new crack surfaces are formed [28].

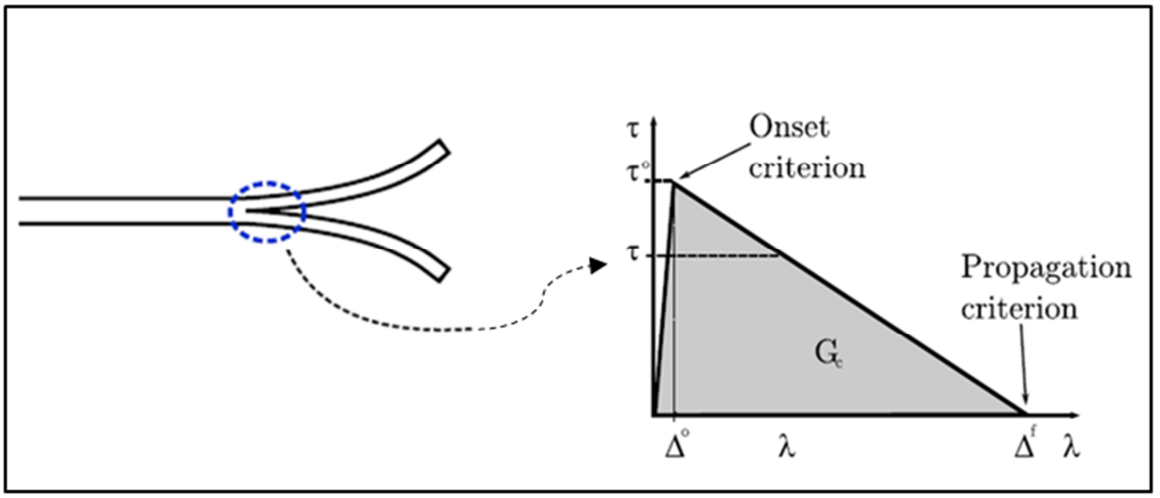

Figure 2.11. Tractions in the cohesive zone ahead of the crack tip.[8]

The advantages and disadvantages of the VCCT and the cohesive zone method are compared in Appendix A.

1.8. FATIGUE LOADING AND CHARACTERIZATION OF FATIGUE-DRIVEN DELAMINATION

Fatigue loading on a material or component results in damage and fracture due to cyclic loading. The key parameters used to describe a cyclic load are shown in Figure 2.12 where the loading is considered as an applied stress but could also be expressed as an applied total load or an applied displacement.

In the case of cyclic loading it is important to distinguish two different regimes:

1. Low-cycle fatigue.
2. High-cycle fatigue.

The first regime is characterized by high stress levels and a relatively small number of cycles to failure (from hundreds to thousands). In contrast, the second one is characterized by low stress levels and a large number of cycles to failure (usually in the range of millions) [30].

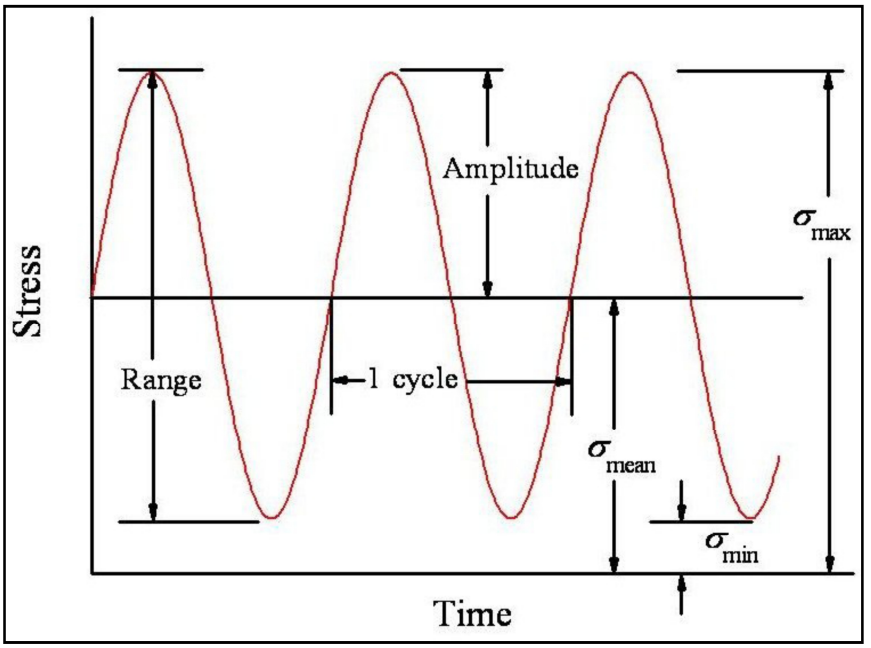

Figure 2.12. Key parameters of cyclic loading [31]

Since fatigue has a very strong effect on the stiffness of composites this can be used to discover how much life they still have. Metals usually retain most of their stiffness under fatigue loading until a high percentage of their life is reached and then it drops suddenly. In contrast, composites in general lose stiffness gradually over their life [32].

Composites go through several stages under fatigue loading. The first is characterized by matrix cracking. The second has coupling of cracks with interfacial debonding as well as some fibre breaking. The third stage is where delamination appears in addition to fibre breaking. In the fourth one delamination growth is present along with localized fibre breaking. The fifth and final stage is where there is gross fracture of the entire material [32].

1.9. FATIGUE GROWTH OF INTERLAMINAR CRACKS

Delamination under fatigue conditions basically involves the same micro mechanisms and processes as under static loading. Then, there is also an initiation or onset process of the delamination and a crack growth or propagation process due to the fatigue

loading. Most of the studies are devoted to the issue of the interlaminar crack propagation while fatigue delamination onset has received less attention. Two different important values of the material fracture toughness have to be taken into account in a fatigue analysis. The first one is related to the critical energy release rate, G_c, which corresponds to the static onset of the delamination. The second one is related to the energy release rate value below which additional interlaminar crack growth is negligible. This value corresponds to the threshold energy release rate, G_{th}, necessary to cause fatigue delamination onset. Below this value, the growth of an interlaminar crack is negligible.

As mentioned, most of the fatigue delamination studies are devoted to the progressive growth of interlaminar cracks under cyclic loading. The crack growth is studied as a function of the number of cycles for a certain reversion index, R. Usually, the well-known Paris law, commonly used for fatigue of metals and progressive crack growth, is used to characterize the delamination growth rate as a power law function of the applied energy release rate. In its simplest form the Paris law can be expressed as

$$\frac{da}{dN} = C\Delta G^r \tag{2.7}$$

where da/dN is the propagation rate of the delamination, a is the delamination length, N is the number of cycles and G is usually taken as the maximum total energy release rate. It is also common to use the energy release rate range, ΔG, instead of the maximum value of G. The constants C and r are the propagation parameters that must be determined experimentally. C is related to the intercept and r to the slope in a Paris plot. The exponent r for composite materials can be about an order of magnitude larger than most metallic materials (Schön et al., 2000; Sjögren and Asp, 2002). Therefore, the predicted propagation rate is very sensitive in the accuracy of the estimated energy release rates. In equation 3.1 G does not discriminate the individual contribution of the different modes. For pure modes (mode I, II and even III) individual propagation parameters must be determined experimentally. For mixed-modes, either the parameters are determined experimentally or they are inferred from the propagation parameters for pure modes [13].

1.10. DELAMINATION TESTING

Interlaminar fracture toughness can be measured in any sequence of the three fracture modes shown in Figure 2.4. Notably, the most often used is pure mode I (opening) or II (shearing), as well as any combination of both. Mode III (tearing) contributions to real delaminations are generally considered to be negligible [33, 34].

The interlaminar fracture toughness is usually measured using beam-type specimens with the delamination growing parallel to the plies. However, the crack does not always follow the expected path. The variation of energy release rate across the width of the specimen, which turns into a non-straight crack front, is one of the causes. Other causes are the different microscopic details of the fracture path or that the crack may wander and follow fibre-matrix interfaces [13].

During the test, the applied load and corresponding displacement are measured and correlated to the length of the delamination. If stable delamination occurs, these data can be correlated at several points. If unstable delamination appears, only the critical load and displacement can be recorded. From the correlated data, the interlaminar fracture toughness can be determined using some beam theory principles and simple expressions. These simple mathematical expressions are usually sufficiently accurate, however, if a more refined analytical evaluation of the testing configuration is needed other models such as FEM models can be used [13].

1.10.1. Mode I Test

The double cantilever beam (DCB) test has been used since the 1960's to derive experimental mode I interlaminar fracture toughness in composite materials [35]. This test method uses a composite beam like in Figure 2.12, with an initial delamination crack [36]. The initial delamination is then forced to grow by pulling the two beams of the specimen away from each other. This ensures the two beams are loaded as if they were cantilever beams in which the span length increases as the delamination grows. Therefore, as the two arms of the specimen are forced to separate by opening, only mode I propagation is obtained.

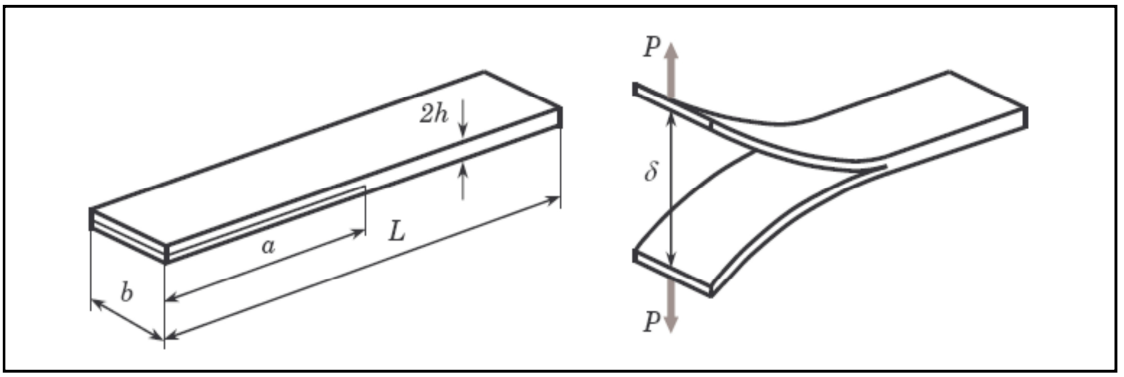

Figure 2.12. Double cantilever beam test in unloaded and loaded conditions [13]

In general, the specimens are manufactured using an even number of plies and placing the first delamination in the mid-plane, in between the central plies. In this way, a mid-plane delamination and a symmetric configuration of the arms are obtained, as seen in the Figure 2.12. The initial, or starter, delamination is introduced into the laminate by a thin non-stick film, usually made of polymer. It is crucial to use a very thin film (less than 13 µm according to the standards [36] to avoid a resin-rich zone at the tip of the film. Such a zone would result in an incorrect initial value of the interlaminar toughness. The size of the tested specimens is usually taken as at least 125 mm long, 20-25 mm wide and 3-5 mm thick, also according to the same standards.

According to the beam theory approach, the mode I energy release rate as a function of the applied load and the compliance for the DCB test can be respectively determined as

(2.8)

where is the axial modulus of the laminate and h is the half-thickness of the specimen.

Whitney et al. [13, 37] used the DCB test to characterize the fracture toughness of different composite laminates and considered different methods of data analysis. These include area method, standard linear beam theory, shear deformation theory and an empirical method where the exponent of the coordinate length is considered a parameter.

Nicholls and Gallagher [38] characterized the mode I initiation and propagation of interlaminar cracks in laminates containing off-axis plies. Smooth fracture surfaces, without fibre breakage, were found in the interfaces between 0º plies. The fracture surface between off-axis plies showed extensive resin deformation, again without fibre breakage. The encountered critical energy release rate values were higher for multidirectional laminates than for unidirectional. In the interface of some off-axis plies the crack grew into another layer with fibre breakage leading to high values of G_c.

1.10.2. Mode II Test

Mode II delamination, or shearing mode, is related to the relative sliding movement of both crack surfaces. The mode II crack propagation in composite laminates is accompanied by the formation of a damage zone, matrix microcracks ahead of the crack tip, which finally coalesce. Therefore, it is difficult to define the real crack length. Friction between the sliding surfaces is another inhibiting factor. These problems turn into a great variability in the results obtained in mode II. As a consequence, a single G_{IIc} value as a material property may be difficult to obtain [39].

Two experimental methods are commonly used to obtain mode II interlaminar fracture toughness: the three-point loaded end-notched flexure (ENF) test and the end-loaded split (ELS) test method. Both of them are based on the monitoring of the delamination growth in a composite beam when an initial delamination is forced to propagate by shearing. In this way, only mode II interlaminar crack propagation is obtained. The preparation of the specimens and the inclusion of the initial or starter delamination are rather similar to the described for the DCB test.

1.10.3. Mixed-Mode I/II Test

Taking into account that delamination is likely to grow in a combination of modes in laminated structures [40], mixed-mode I/II delamination tests are of great interest for the determination of interlaminar fracture toughness. In addition, as many composite failures involve mixed-mode I/II, with mode I dominant over mode II, and the determination of

mode II fracture toughness involves some intrinsic problems, it is stated that mode I and mixed-mode I/II test methods are more useful for the prediction of delamination failure in composite structures [39].

Diverse experimental methods to obtain the mixed-mode I/II interlaminar fracture toughness of a laminate or fatigue sub-critical propagation exist. The more relevant and most commonly used are the mixed-mode bending (MMB) and the mixed-mode end load split (MMELS) test methods. Both of them are based on the monitoring of the delamination growth starting from an initial delamination crack in a composite beam. In both cases, the initial delamination is forced to propagate by opening and shearing. The ratio between them depends on the geometry of the specimen and test conditions. As in mode II test, the preparation of the specimens and the inclusion of the initial delamination are rather similar to the described in the DCB test.

1.10.4. MMB Test

The more commonly used is the so-called mixed-mode bending test (MMB). The test, initially proposed by Reeder and Crews [41] and modified afterwards by the same authors [42, 43], uses a symmetrically pre-delaminated specimen generally identical to the DCB specimens. The test allows the determination of the interlaminar fracture toughness with a mixed-mode I/II ratio ranging from almost pure mode I to pure mode II. The test rig is schematically shown in Figure 2.13 with its variables. Different mixed-mode ratios can be obtained with the variation of the loading point on the lever (varying distance c).

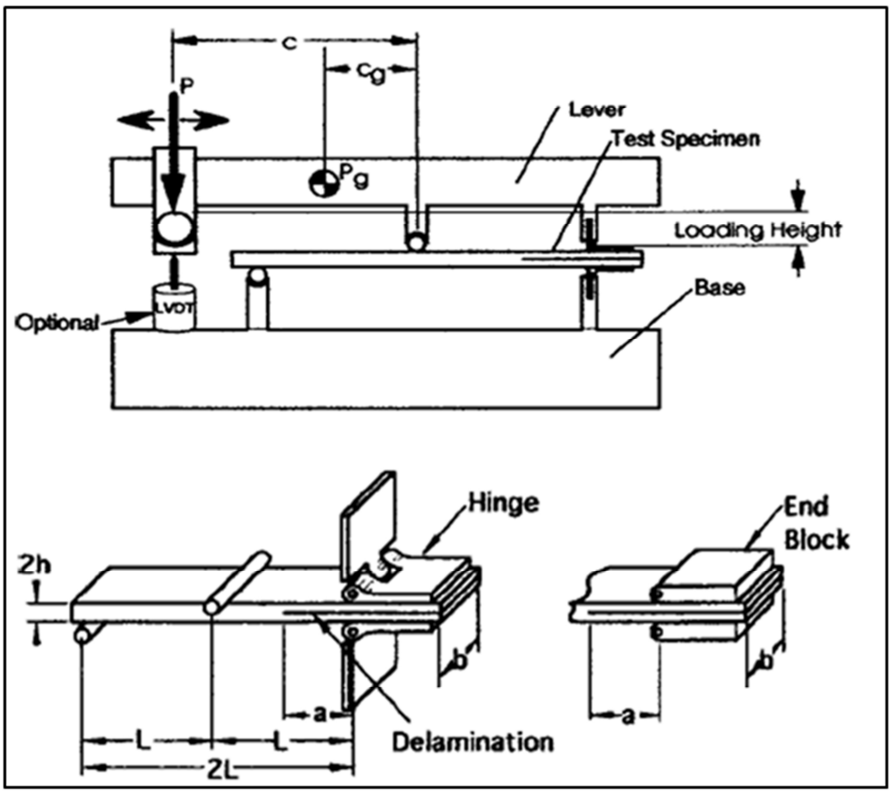

Figure 2.13. MMB Apparatus [43]

During the test, loads are applied to the specimen through end blocks or piano hinges bonded to the specimen beams at the delaminated end. The rollers at the non-delaminated area reduce the friction forces. The underside end block or piano hinge is fixed to the base of the rig and the other extreme of the specimen is supported by a roller. When a downward load is applied on the lever arm, a downward force is applied in the central part of the specimen meanwhile the upper end block or piano hinge is pulled up. To ensure that the load applied on the lever arm remains vertical, a saddle and yolk arrangement is used in combination with rollers to reduce friction loads. To avoid nonlinear effects as the lever rotates, it is vital to ensure that the loading point is slightly above of the mid-plane of the specimen [44]. Figure 2.14 shows the MMB apparatus manufactured and used in this study.

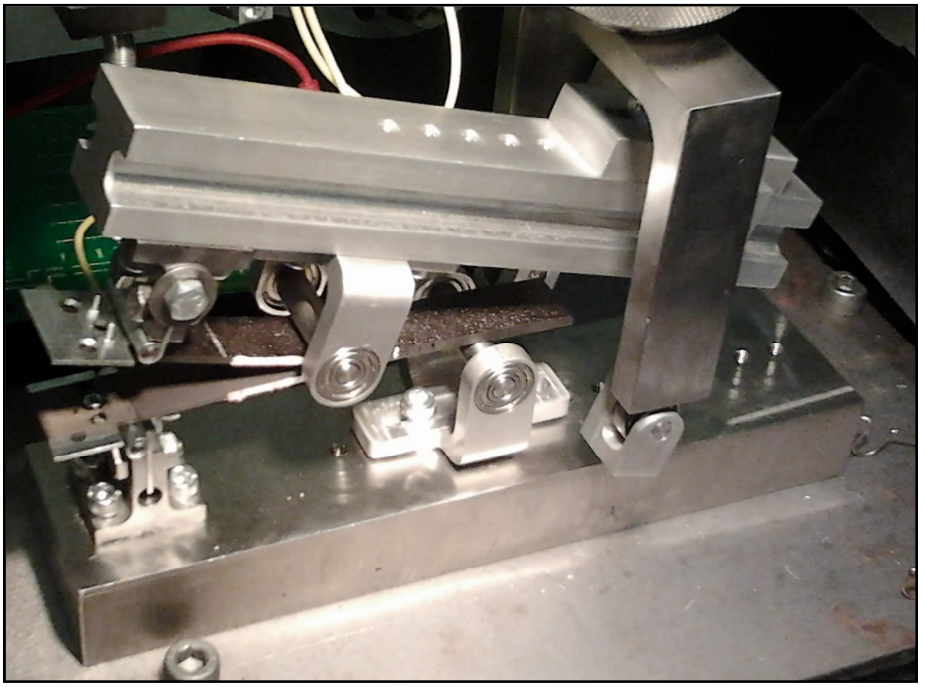

Figure 2.14. MMB Apparatus used in this study

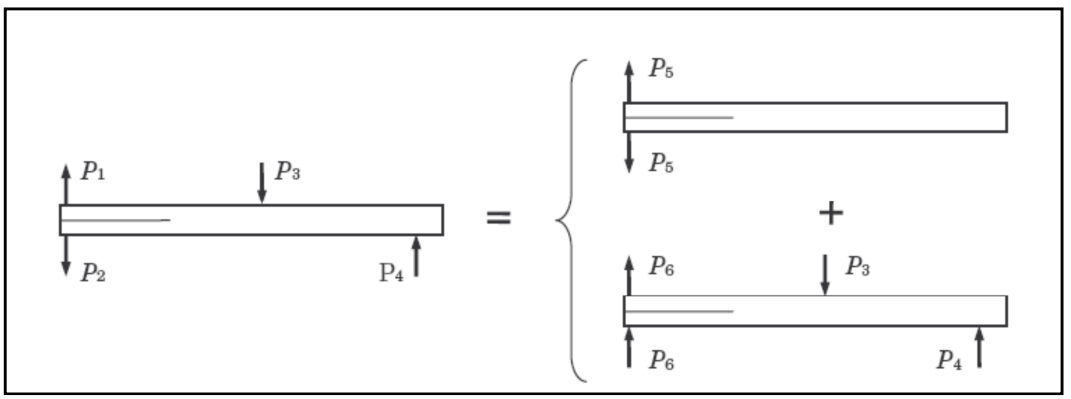

Figure 2.15. MMB test as superposition of DCB and ENF tests [13]

As shown in Figure 2.15, the MMB test can be treated as the superposition of a mode I DCB test and a mode II ENF test. According to this superposition the different loads can be expressed as functions of the applied load P and test configuration as

– (2.9)

$$P_2 = P\left(\frac{c+d}{2L} - 1\right) \tag{2.10}$$

$$P_3 = P\left(\frac{c+L}{d}\right) \tag{2.11}$$

$$P_4 = p\frac{c+d}{2L} \tag{2.12}$$

$$P_5 = \frac{P}{2}\left(\frac{c-d}{d} + \frac{c+d}{2L}\right) \tag{2.13}$$

$$P_6 = \frac{P}{2}\left(\frac{c+d}{d} - \frac{c+d}{2L}\right) \tag{2.14}$$

Taking into account the superposition shown in Figure 2.14 and according to the beam theory approach, the mode I and mode II energy release rates as functions of the applied load and the compliance of the system for the MMB test can be respectively determined as

$$G_I = \frac{3P^2a^2}{b^2E_{11}h^3}\left(\frac{c+d}{2L} - 1 + \frac{c}{d}\right)^2 \tag{2.15}$$

$$G_{II} = \frac{9P^2a^2}{4b^2E_{11}h^3}\left(\frac{c+d}{2L} - 1 - \frac{c}{d}\right)^2 \tag{2.16}$$

$$C = \frac{a^3}{4b\ \ E_{11}h^3}\left|8\left(\frac{c+d}{2L} - 1 + \frac{c}{d}\right)^2 + 6\left(\frac{c+d}{2L} - 1 - \frac{c}{d}\right)^2 + \frac{d^2(2L-d)^2}{L}\left(\frac{c+d}{2L} - 1 - \frac{c}{d}\right)^2\right| \tag{2.17}$$

where the last term in the square-parenthesis corresponds to the compliance of the system without delamination. Then, the energy release rate can also be obtained as a function of the displacement as

$$G_I = \frac{3\delta^2 E_{11} h^3}{4a^4 \left(\frac{c+d}{2L} - 1 + \frac{c}{d}\right)^2} \tag{2.18}$$

$$G_{II} = \frac{9\delta^2 h^3 a^2}{\left(3a^2 \frac{d^2(2l-d)^2}{L}\right)^2 + \left(\frac{c+d}{2L} - 1 + \frac{c}{d}\right)^2} \tag{2.19}$$

Usually, and according to the standards ASTM 6671-01 [45], the distance d is taken as L. In this way, all the previous expressions become simpler. However, only a limited range of crack lengths is achieved [45]. When the position of the fulcrum on the lever arm is set to the half span of the specimen, d = L, the mixed mode ratio depends only on the distance c. For short c distances, mode II is predominant. On the other hand, for larger c values, mode I predominates. Nevertheless, if the simple beam theory approach is considered, for a value of c between zero and one third of L, the mode mix, defined by the ratio of the mode II component to the total energy release rate, G_{II}/G varies between 0.42857 and 1, respectively. For larger values of c, the mode mix decreases progressively.

As in the previously described tests, different correction factors to account for the rotation of the beams and large displacement effects can be considered [39, 43, 44].

1.10.5. Loading Systems in Delamination Tests

To avoid undesired effects and to assure the correct application of the external load to composite beam specimens, load should be applied centered to the mid-plane of the beam thickness. However, this is not always possible and different loading systems are used without achieving this requirement. The systems most commonly used to apply the external load to beam specimens in delamination tests are the so-called end blocks and piano hinges. A schema of both systems can be seen in Figure 2.16.

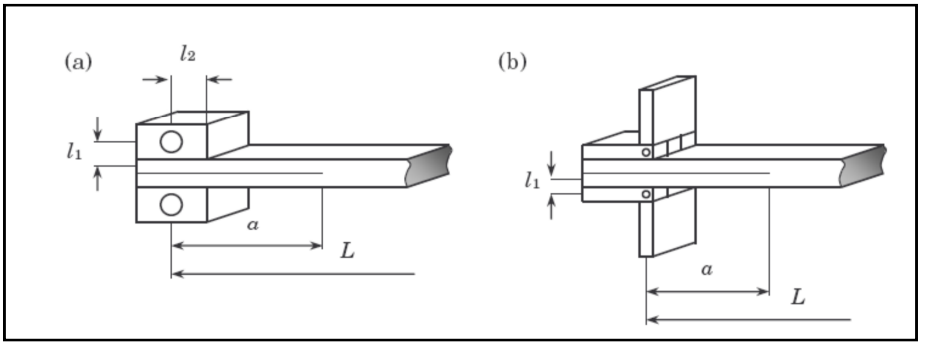

Figure 2.16. Composite beam loaded by a. End block and b. Piano hinges [13]

1.11. MMB DELAMINATION FAILURE CRITERIA

Interlaminar crack onset and growth in pure mode I and mode II is related to the fracture toughness properties of the material. Thus, under pure mode I the critical growth of the crack would be achieved provided the energy release rate of the system is equal to the critical energy release rate under mode I, , of the material. Similarly, crack propagation under mode II would occur provided is equal to . However, when mixed-mode loading is present, a specific failure criterion is needed for crack propagation. Many attempts have been made to describe the mixed-mode delamination failure response of composite laminates. The more commonly used ones are briefly summarized in the following.

As the value of most of the epoxy matrix laminates is lower than the value, it can be considered that most structural delamination failures are controlled by mode I toughness. Therefore, a delamination criterion can be expressed as a function of , except for the cases with a high contribution of mode II, where the criterion is expressed as a function of (Whitcomb, 1986) [46]. The criterion is simple to use and can be written as

(2.20)

Another criterion assumes delamination propagation if the total energy release rate, as the sum of the mode I and mode II components, reaches a critical value [47]. The criterion can be expressed as

$$G_I + G_{II} = G_c \tag{2.21}$$

The so-called linear criterion normalizes each component of the fracture toughness and generates a linear locus between G_{Ic} and G_{IIc}. This mixed-mode criterion is one of the most commonly used and is given by:

$$\frac{G_I}{G_{Ic}} + \frac{G_{II}}{G_{IIc}} = 1 \tag{2.22}$$

The power law criterion is a generalization of the linear criterion that allows for the non-linearity of the fracture toughness locus. The power law criterion is expressed as (Whitcomb, 1986) [46]:

$$\left(\frac{G_I}{G_{Ic}}\right)^m + \left(\frac{G_{II}}{G_{IIc}}\right)^n = 1 \tag{2.23}$$

where *m* and *n* are material parameters that must be determined experimentally. When the values of *m* and *n* are higher than unity, the locus is convex, while when *m* and *n* are less than unity, the failure locus is concave. If $n > m$, the locus is skewed towards the mode I axis. The case of $m = n = 1$ coincides with the linear criterion.

Based on the study of laminated materials and bimaterial interfaces, Hutchinson and Suo (1992) assumed that the fracture toughness of the interface between the plies where the delamination grows depends on the mode mix[48]. The authors described the variation of the critical energy release rate as

$$G_c = \frac{G_{Ic}G_{IIc}}{G_{IIc} + (G_{Ic} - G_{IIc})\sin^2\psi} \tag{2.24}$$

where the mode mix angle ψ is defined as

$$\psi = \arctan\left(\frac{K_{II}}{K_I}\right) \tag{2.25}$$

The criterion proposed by Benzeggagh and Kenane [49] is one of the most widely used one. The criterion is based on the stress intensity factor around the delamination crack tip and can be expressed as a function of the energy release rates as given below.

$$G_I + G_{II} = G_{Ic} + (G_{IIc} - G_{Ic})\left(\frac{G_{II}}{G_I + G_{II}}\right)^m = 1 \tag{2.26}$$

where the constant *m* must be determined experimentally. Additionally, a variation of the previous expression is used in which the denominator $(G_I + G_{II})$ is replaced by G_{IIc}.

1.12. TAPERED LAMINATES

Tapered composites formed by terminating or dropping of some of the plies in some primary structures have received much attention from researchers since the mid-1980s. Their elastic tailoring properties and potential for creating more significant weight savings than commonly-used laminated components allow an increasing use of the tapered composites in commercial and military aircraft applications.

A typical example is the helicopter yoke, shown in Figure 2.17 where a progressive variation in the thickness of the yoke is required to provide high stiffness at the hub and relative flexibility at the mid-length of the yoke to accommodate flapping.

Constructed completely from S-2 glass, the dual-yoke assemblies on the Bell 430 helicopter endure several times more flight hours than traditional titanium or steel yokes, and also provide improved safety. Much more tolerance to damage than conventional materials and the elimination of corrosion are also displayed by these composite components. Other applications include composite aircraft-wing skins, helicopter flex beams, fly-wheels, etc.

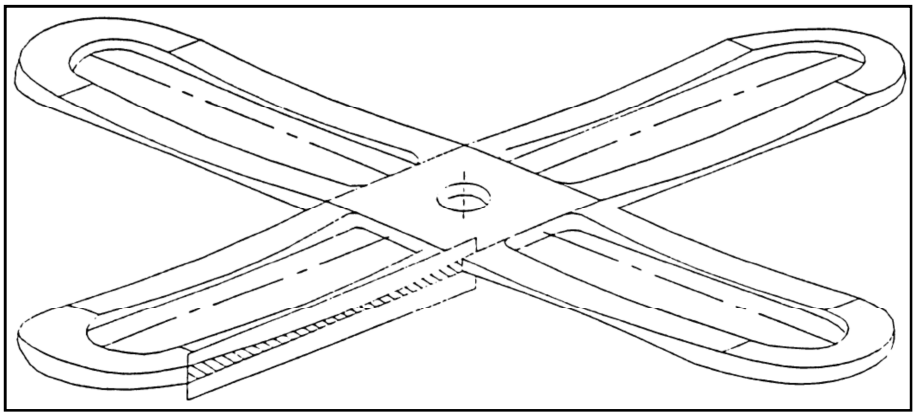

Figure 2.17 Helicopter yoke [50].

Tapered composite structures, being formed by terminating some of the plies, have material discontinuities that act as sources for delamination initiation and propagation. The delamination mechanisms in tapered laminate composites have been a difficult task for researchers for more than a decade. The difficulties in modeling tapered composite structures for stress analysis, and delamination initiation and growth lie in their geometric and material discontinuities as well as the free-edge effect. All of these would produce a complicated stress distribution around the ply drop-off region.

There are several basic types of tapers that are often used and analyzed, and they are identified in Figure 2.18 and an example for taper with internal ply drops can be seen in Figure 2.19. In addition, A table of the summary of important papers on tapered laminates can be found in [50].

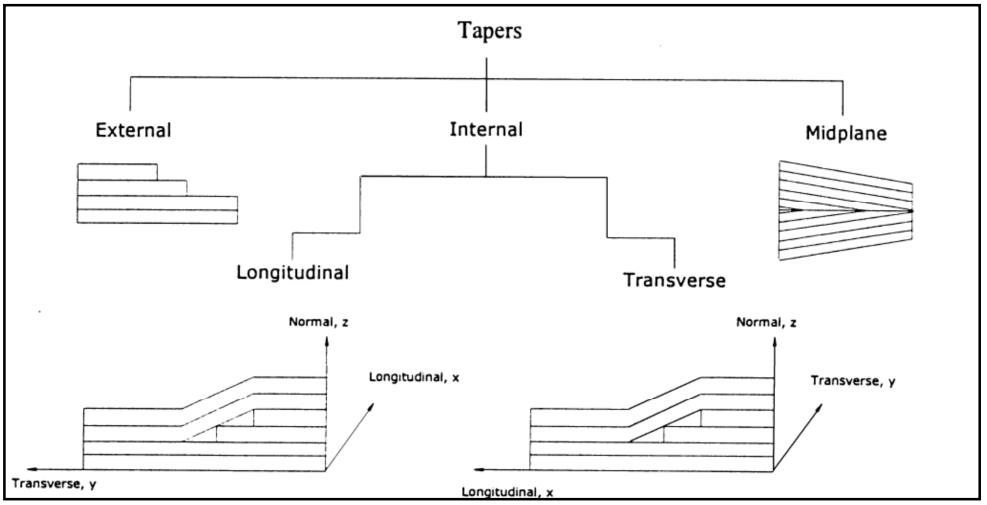

Figure 2.18. Basic types of tapers with dropping plies [50]

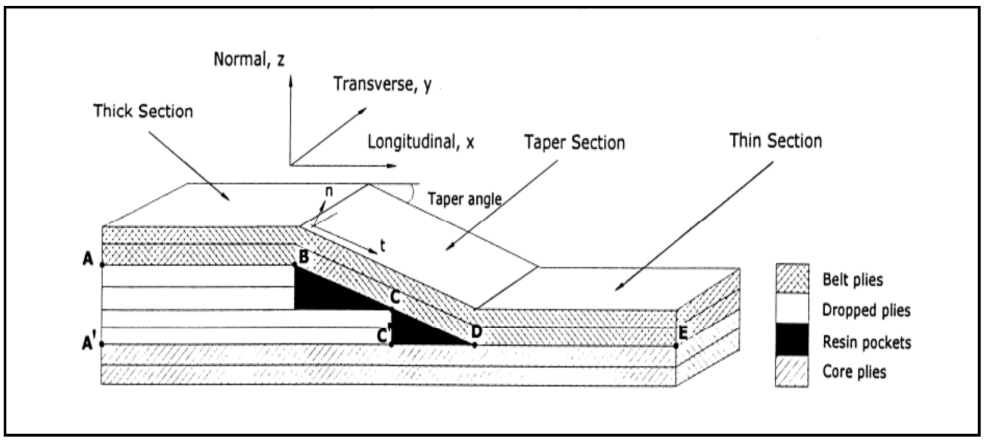

Figure2.19. Schematic of taper with internal dropped plies [50]

EXPERIMENTAL WORK

1.13. MATERIAL

The material used to produce the test specimens is carbon-fiber reinforced UD (unidirectional) pre-preg tape, which is epoxy-resin impregnated, manufactured by Hexcel. The tape is of Standard-Modulus type. The resin is HEXPLY® F584™ and the fiber is AMOCO T650/35-12K. Hexcel designation for the prepreg tape is T7G145-12"-F584, which has a standard width of 12 inch (305 mm). The areal weight of the fiber is 145g/m^2. The resin content of the tape is 35-39 %. According to the product flyer, a fiber volume fraction of 55 % is attained when tapes are manufactured into a laminate with the standard cure process. The neat resin and mechanical properties as specified by the company can be found on their web site [51]. The test specimens for this work were manufactured by TAI (Turkish Aerospace Industry) using their own material supplies.

1.14. MANUFACTURING PROCESS

The laminated plates, from which the test specimens were to be cut, were manufactured by TAI using the vacuum bagging technique. They used a cure temperature of 177 °C (350 °F). The standard cure cycle for this material is given in Figure 3.1. For the tapered plates, the flat side faced down and, hence, was in contact with the tooling. The tapered side faced the vacuum bag and was, therefore, the rough side after curing. TAI used nameplates (small flat pieces of metal) on the inclined taper region to ensure a precise and smooth taper. Three tapered plates with different layup configurations were manufactured.

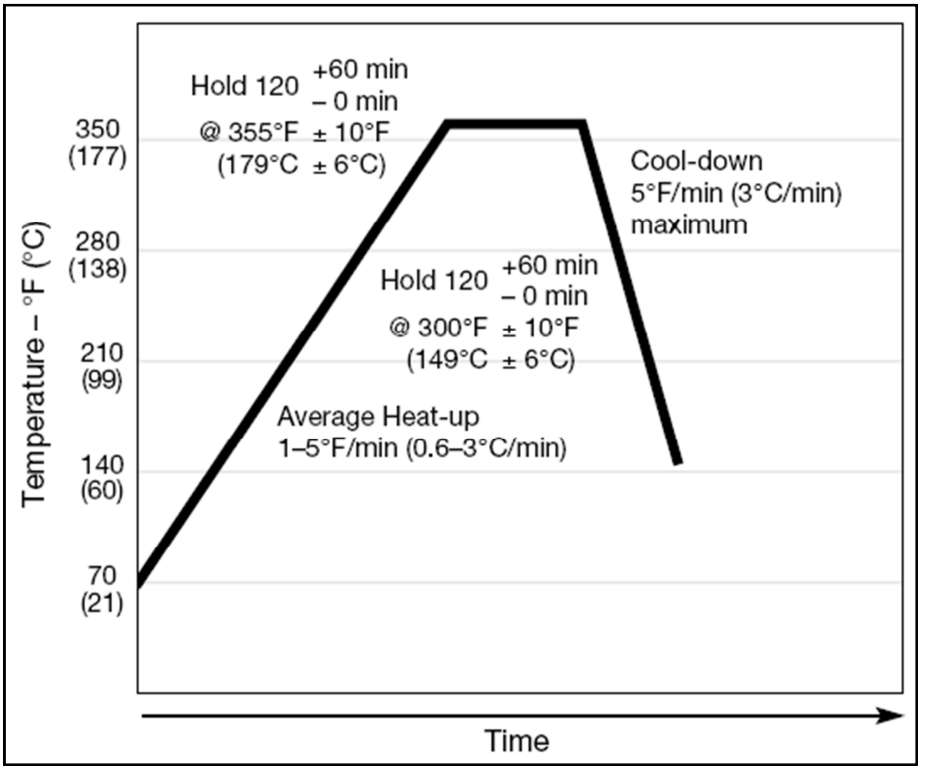

Figure 3.1. The standard cure cycle for the presented material [51]

Altogether six plates, three of which were tapered, were manufactured for the tests. The following is a description of these plates:

- A 278x177 mm^2 UD laminated uniform-thickness plate of 12 plies to be used for delamination (fracture) toughness tests: had a 20 mm wide teflon insert on one of the long sides of the plate to act as initial delamination. The teflon was to be inserted in the mid-plane between plies 6 and 7. The plate was cut into test coupons (strips) with a diamond coated circular cutter which had a cutting thickness of 4 mm and a trade name of SK450 manufactured by Yılmaz Machine Co. in İstanbul. It was discovered that the insert was not placed symmetrically and the orientation of the plies (fibers) was not perpendicular to the delamination front, but parallel to it, that is, the plate was a 90° plate. This plate was, therefore, not usable for delamination toughness tests.
- A 278x179 mm^2 UD laminated uniform-thickness plate of 28 plies to be used for delamination (fracture) toughness tests: had a 50 mm wide teflon insert on one of the long sides of the plate to act as initial delamination. The teflon was inserted in the

mid-plane between plies 14 and 15. This plate was manufactured to replace the first delamination plate described above. The plate was cut into 20-mm wide test coupons by water-jet technology, which had a 1.5 mm cutting thickness, in İMES (İstanbul Metallic Goods Manufacturers Complex). 11 toughness specimens were obtained for DCB and MMB tests.

- Three 270x220 mm^2 tapered plates each with a distinct stacking sequence: had 14 plies in the thick part and 8 in the thin part, hence, had 6 plies dropped. The taper was achieved in a distance of 8.4 mm corresponding to a taper angle of 5.7° in Figure 3.2. The stacking sequences are shown in Table 3.1. The plates were trimmed and cut into 25.4 mm wide and 227 mm long coupons. Six clean coupons were obtained from each plate, giving a total of 18 specimens to be used in fatigue tests. Initially 50 mm long aluminum tabs produced at Yeditepe University were adhesively bonded to each end of the coupons giving a net test section of 127 mm. TAI reported that bonding between the composite and the aluminum tabs was not achieved because of differential expansion during temperature curing of the adhesive. They recommended and used glass-fiber composite tabs instead of aluminum ones.
- A 230x170 mm^2 UD laminated uniform-thickness plate of 8 plies to be used for simple tension testing: TAI bonded 50 mm wide glass-fiber composite tabs on each side of the plate which was then cut into five 25.4-mm-long coupons in İstanbul with the diamond coated circular cutter SK450.

The tapered specimen geometry and the stacking sequence of the three plates are given in the figures and table below. Subscript D indicates the dropped (discontinuous) plies.

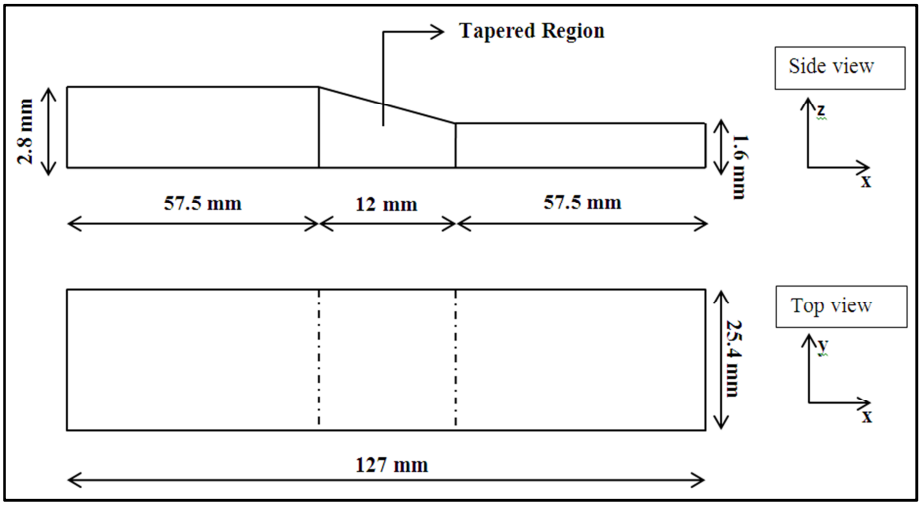

Figure 3.2. Tapered specimen geometry

Table 3.1. The stacking sequences of the tapered plates

TL1	$0/0/90/90/+45_D/-45_D/0_D//0_D/-45_D/+45_D/90/90/0/0$
TL2	$0/0/90/90/+45_D/-45_D/+45_D//+45_D/-45_D/+45_D/90/90/0/0$
TL3	$0/0/90/0/+45_D/+45_D/0_D//0_D/-45_D/+45_D/0/90/0/0$

The 0^o and 90^o tension specimen (UD1 and UDT1) geometries and the measured values of the dimensions are given in Figures 3.3 and Tables 3.2-3.5.

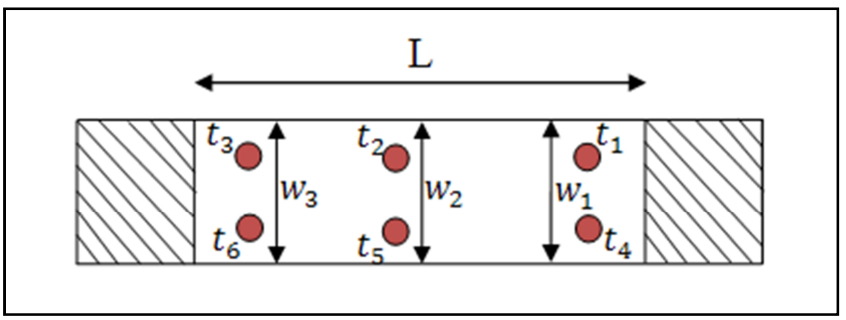

Figure 3.3. Tension test specimen geometry for 0^o and 90^o orientations

Table 3.2. Dimensional parameters for 0^o oriented specimen UD1 in Figure 3.3

i	**1**	**2**	**3**	**4**	**5**	**6**
w_i (mm)	25.7	25.75	25.5	-	-	-
t_i (mm)	1.4	1.35	1.36	1.4	1.36	1.35

Table 3.3. Average dimensions for the 0° oriented specimen UD1

L (mm)	**w_{ave} (mm)**	**t_{ave} (mm)**
135	25.65	1.36

Table 3.4. Dimensional parameters for 90° oriented specimen UDT1 in Figure 3.3

TABLO	**1**	**2**	**3**	**4**	**5**	**6**
w_i (mm)	20.3	20.2	20.2	-	-	-
t_i (mm)	40	40.1	40.15	40.1	40.1	40.1

Table 3.5. Average dimensions for the 90° oriented specimen UDT1

L (mm)	**w_{ave} (mm)**	**t_{ave} (mm)**
80	20.2	40.1

The measured dimensions of the 12 fracture-toughness (DCB and MMB) specimens and of the 18 tapered specimens are shown in Tables 3.6 and 3.7, respectively. The bold values in Table 3.7 (TL2f, TL3f) indicate the two tapered specimens which were tested statically. The reasons for these tests were to get an idea about the load levels to apply in the fatigue tests. The results of these static tests are given in Table 3.8. Only the fracture force and average stress are given in the table since the crosshead displacement measurements were not reliable. The average failure stress in the Table 3.8 is simply the failure load divided by the cross-sectional area of the thin part. As expected, configuration TL3 is stronger than TL2.

Table 3.6. Average dimensions of the fracture-toughness test specimens

No	Specimen Code	Thickness (mm)	Width (mm)
1	**a**	4.4	20.10
2	**b**	4.4	20.20
3	**c**	4.4	19.90
4	**d**	4.4	20.10
5	**e**	4.4	20.00
6	**f**	4.4	20.15
7	**g**	4.4	20.05
8	**h**	4.3	20.15
9	**i**	4.3	20.10
10	**j**	4.4	20.05
11	**k**	4.4	20.10
12	**l**	4.5	20.20

Table 3.7. Average dimensions of the tapered specimens

Specimen	Width(mm)	Ta (mm)	Tb (mm)
TL 1a	25.7	1.7	2.8
TL 1b	25.7	1.8	2.9
TL 1c	25.6	1.7	2.8
TL 1d	25.7	1.7	2.8
TL 1e	25.7	1.6	2.8
TL 1f	25.5	1.7	2.8
TL 2a	25.5	1.8	2.8
TL 2b	25.6	1.7	2.8
TL 2c	25.5	1.7	2.8
TL 2d	25.6	1.8	2.8
TL 2e	25.6	1.7	2.8
TL 2f	**25.6**	**1.7**	**2.8**
TL 3a	25.6	1.8	2.8

Table 3.7. Average dimensions of the tapered specimens (continue)

Specimen	Width(mm)	T_a (mm)	T_b (mm)
TL 3b	25.6	1.8	2.8
TL 3c	25.6	1.8	2.9
TL 3d	25.7	1.7	2.9
TL 3e	25.7	1.8	2.9
TL 3f	**25.7**	**1.8**	**2.9**

Table 3.8. The static test results of the tapered specimen

Configuration	Failure Load (N)	Failure Stress (MPa)
TL2f	22954	527.44
TL3f	44851	969.52

1.15. EXPERIMENTS

1.15.1. Unidirectional tension tests

Standard tension tests were carried out as per ASTM standard D3039 to determine the moduli and Poisson's ratios for the composite material used in the study. There were five standard 0° UD samples from which E_{11} and ν_{12} were determined. The original delamination-toughness samples were not usable for reasons described above. Instead some of them were trimmed to cut off the delaminated parts and used as 90° UD samples even though these samples were not of standard size. E_{22} and ν_{21} were determined from the 90° tests and the equality ν_{12}/ E_{11} and ν_{21}/ E_{22} was verified from the two types of tests. The universal testing machine used was Instron 3382 of 100 kN capacity which belongs to the Department.

1.15.1.1. Test Procedure

The tests were conducted at a loading rate of 0.5 mm/min as dictated by the standard. A pair of strain gauges was bonded to one of the lateral surfaces of the specimen in the

middle. Hence the gauges read the 0° and 90° (longitudinal and lateral) strains. The gauges were of type 3/120XY11 manufactured by HBM, which had a nominal resistance of 120 Ω and a nominal gauge factor of 2.01± 1 %. In addition, an extensometer was used to cross check the longitudinal strain gauge reading. Good alignment of the specimen with respect to the Instron machine was ensured by marking the vertical midline of the tabs and of the jaws of the machine and by fixing the location of the specimen with the help of the marking lines. A laser bubble level was also used to check the alignment.

A data acquisition (DAQ) system, Nic 9237, connected to the desktop computer of the testing machine was used to receive the strain gauge data. Quarter bridge configuration of the DAQ system was used. The software of the DAQ system writes the data received in an excel file. The system has a sampling rate of 1612 Hz. On the other hand, a sampling rate of 10 Hz was chosen for the testing machine. Synchronous triggering of the DAQ system and the testing machine was an issue to be careful about. The reason for this concern is that the DAQ system writes the absolute time of each sampling in the excel file whereas the time output of the software of the testing machine is relative to the start of the testing. This issue was resolved as follows: The software of the DAQ system was set to begin sampling and writing data at a certain time and the testing machine was manually started at the same time instant. Seeing the windows for both of the software simultaneously on the screen, it was thought that the timing error was under a second.

1.15.1.2. Test Results

The stress-strain curve for 0^o specimen UD1 is shown in Figure 3.4. The strain is the output of the strain gauge and the stress is computed by the testing machine. Figure 3.5 shows a plot of the transverse strain vs. axial strain for UD1, from which the major Poisson ratio is computed.

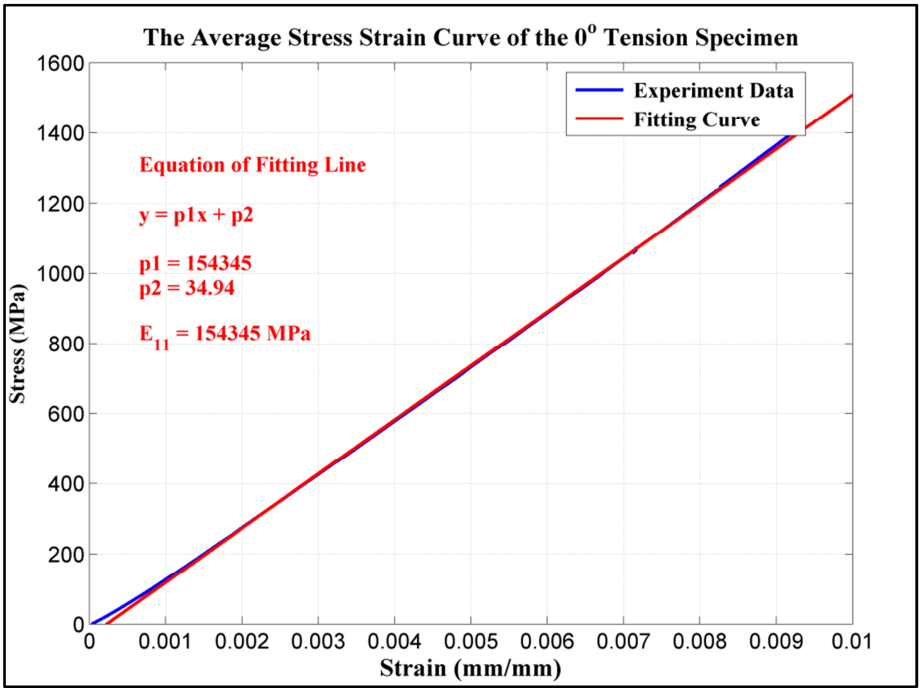

Figure 3.4. The average stress-strain curve of the 0° specimen UD1

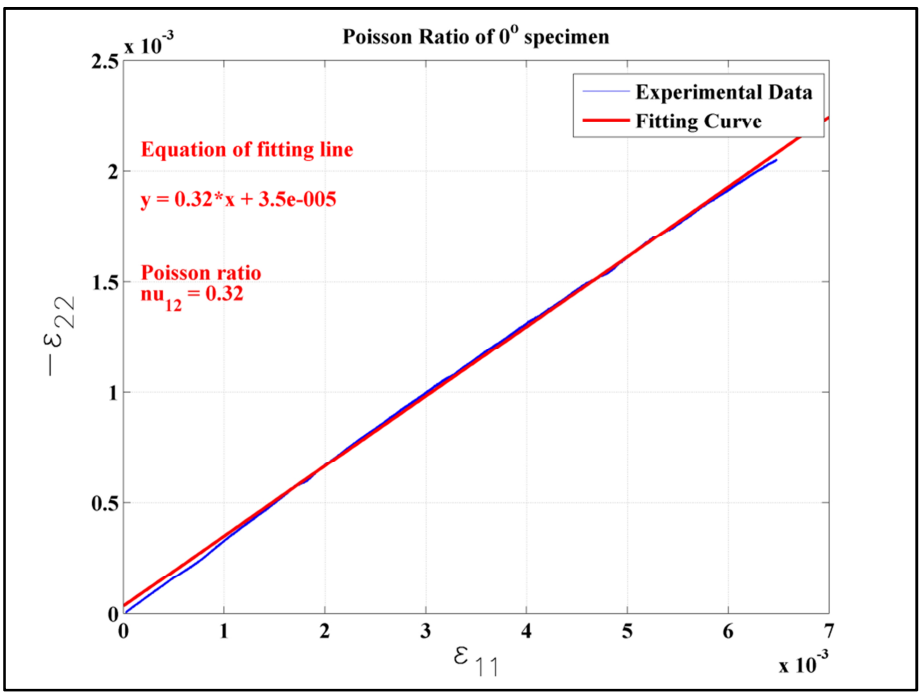

Figure 3.5. Transverse vs. axial strain curve of the 0° specimen UD1

The stress-strain curve for 90° specimen UDT1 is shown in Figure 3.6. Figure 3.7 shows a plot of the transverse strain vs. axial strain for UDT1, from which the minor Poisson ratio is computed. The ratios of E_{11}/ and E_{22}/ are computed from Figures 3.5 and 3.7. The error between these ratios is quite small (an error of % 3.3), which shows that the tests are reliable.

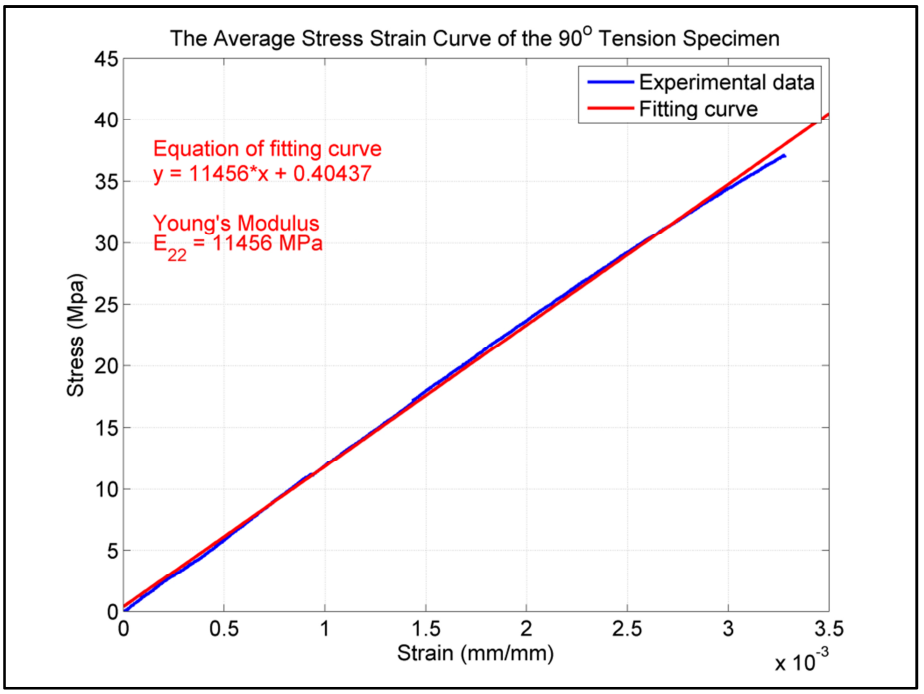

Figure 3.6. The average stress-strain curve of the 90° specimen UDT1

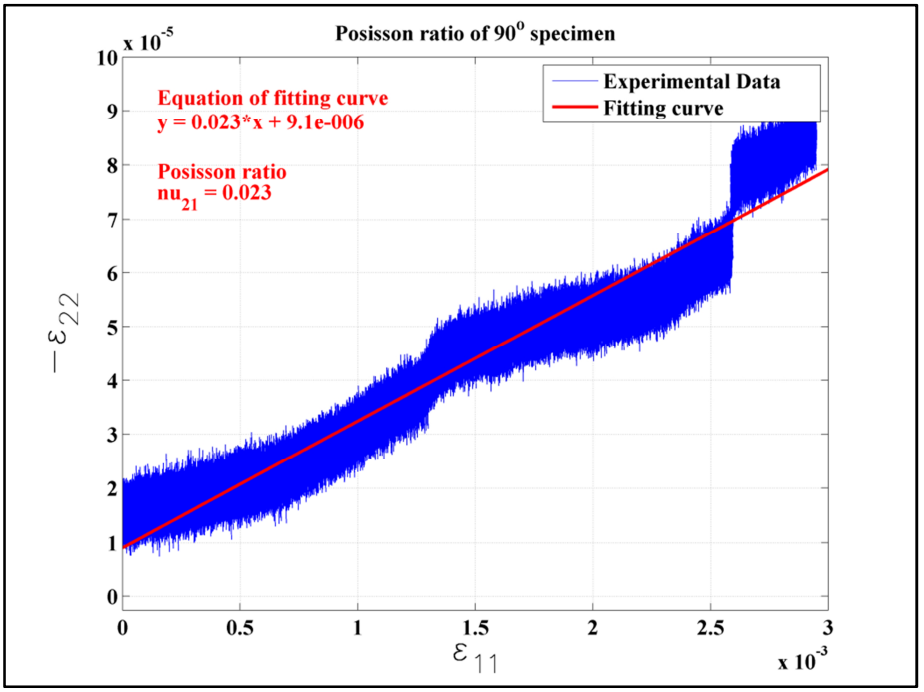

Figure 3.7. Transverse vs. axial strain curve of the 90° specimen UDT1

1.15.2. Three Point Bending Test

The three point bending test is conducted with a loading rate 0.5 mm/min. Two specimens were tested, which were nominally the same as the tension test specimens. Figure 3.8 shows the force applied and the resulting displacement in the middle of one of the specimen.

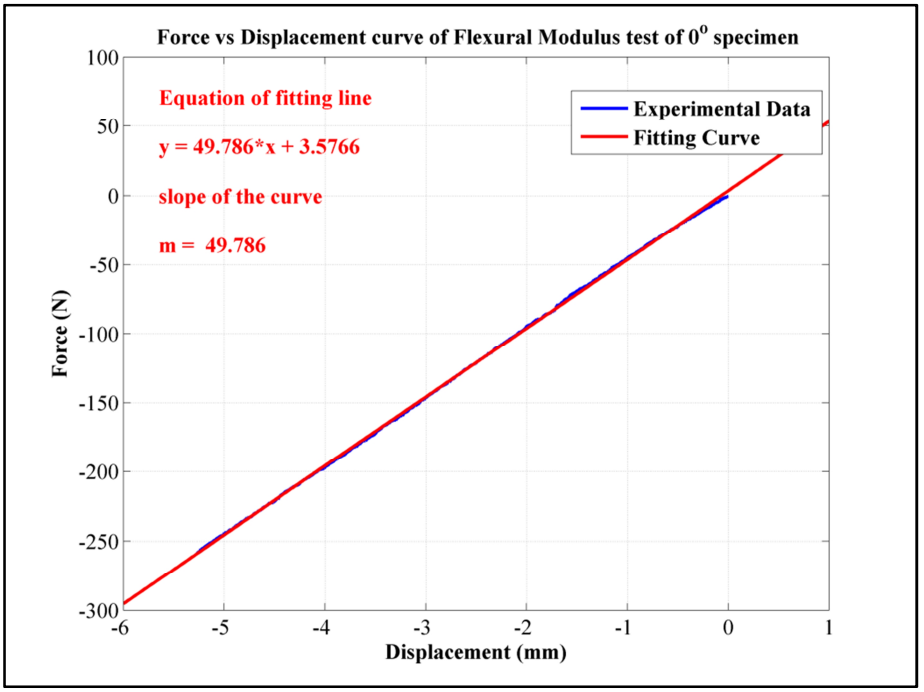

Figure 3.8. The load-displacement curve of the experimental data for flexural test

The flexural modulus equation is shown below,

(3.01)

where is the flexural modulus, S the span, m the slope of the fitting line, b the width and h the thickness of the specimen. According to the equation 3.01, flexural modulus of the 0^o specimen is 105868 MPa.

1.15.3. DCB Tests

1.15.3.1. Test Procedure

These tests are conducted at a loading rate of 0.5 mm/min. The specimens are bolted to the hinges as seen in Figure 3.9. The alignment of the specimen relative to the machine is ensured by marking the hinges and the clamps of the machine with pens. A small bubble level is used on the specimen to level the specimen.

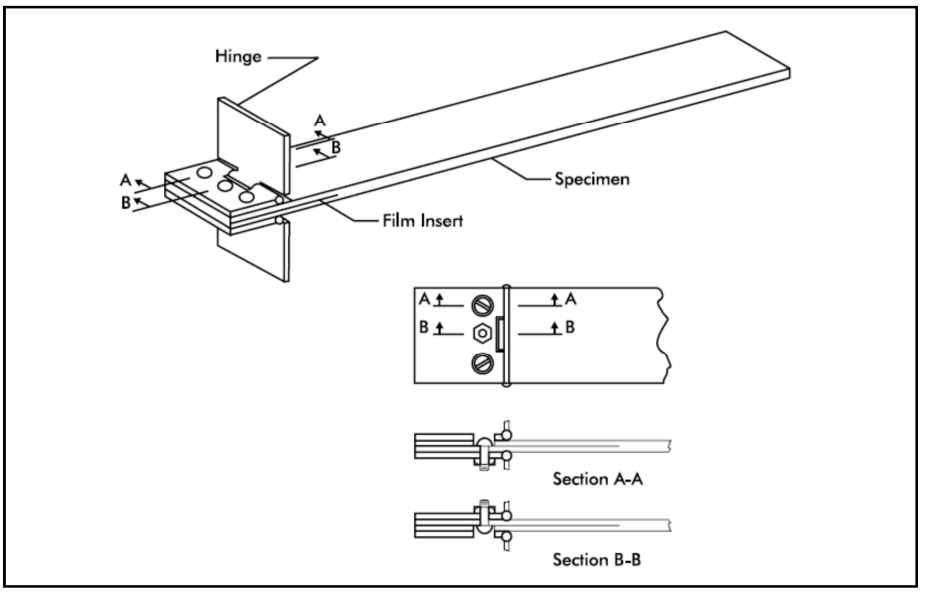

Figure 3.9. DCB specimen with hinges attached by bolting [52]

After they are well aligned the displacement is obtained by a fixture which includes a multi-meter Agilent 34410A, a board and a FEEDBACK variable resistor with a FEEDBACK power supply. As the measurement of the crosshead displacement by the machine was not reliable, a metal strip was connected between the crosshead and a variable-resistance displacement transducer and the displacement was measured independently of the machine. The metal strip and the variable resistor can be seen to the right of the jaws and the load cell in Figure 3.10. The Agilent 34410A multi-meter has an interface on pc which provides triggering at a known time. Therefore, triggering is provided by starting the test at the same time as the data acquisition. One sample per second is obtained from both during the test.

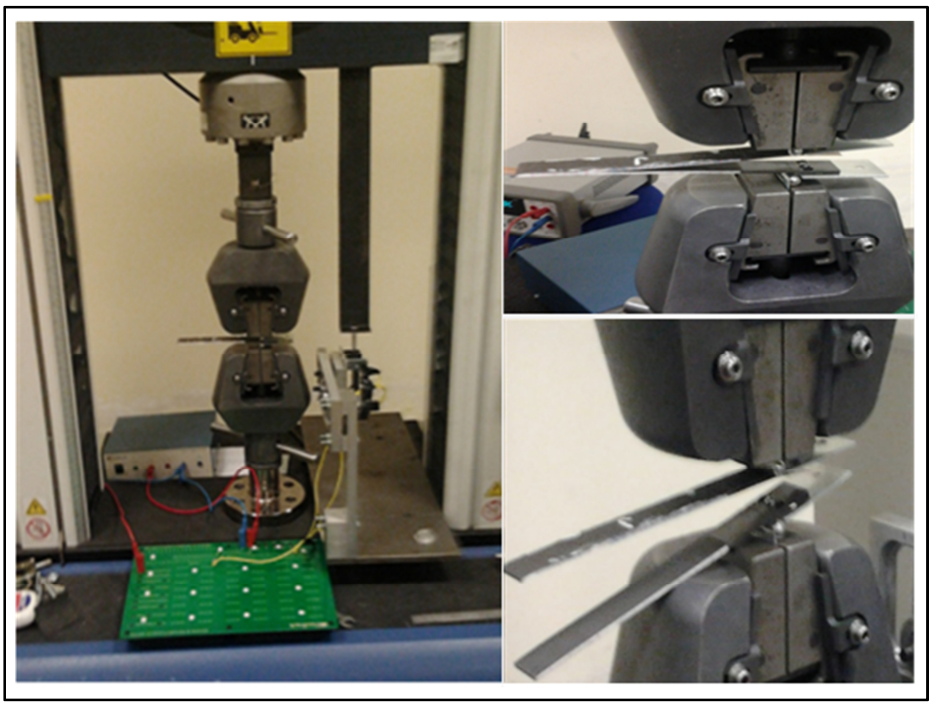

Figure 3.10 The DCB test rig

1.15.3.2. Test Results

Two specimens J and I used for the DCB Mode 1 test. The reaction force-displacement curve for fracture toughness specimens “J and I” is shown in Figure 3.11. The Displacement is the output of the variable resistor and the reaction force is computed by the testing machine.

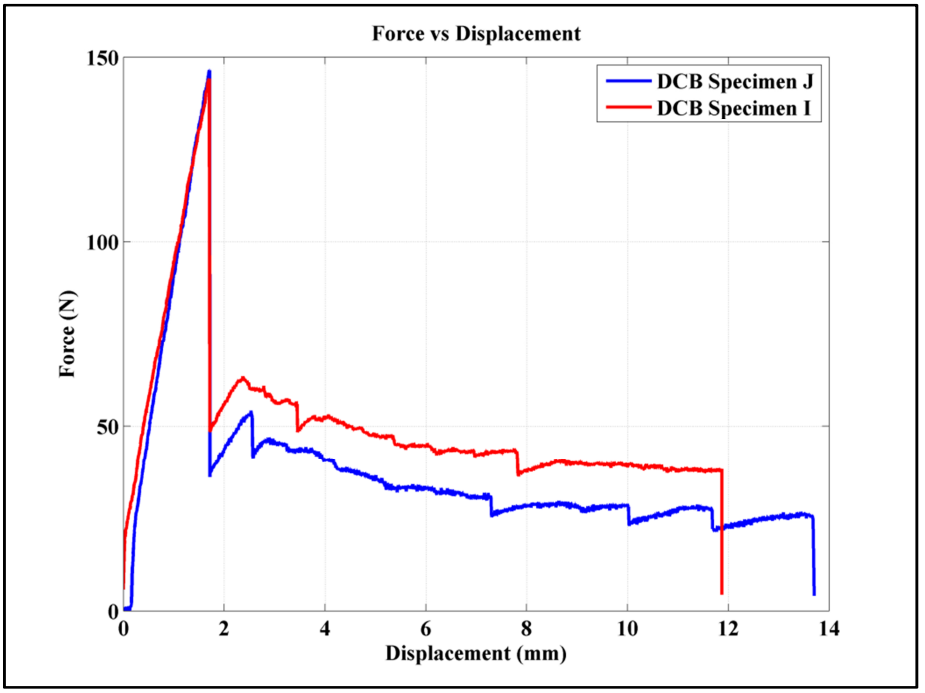

Figure 3.11. DCB test results of the two specimens

1.15.4. MMB Test

1.15.4.1. Test Procedure

These tests are conducted at a loading rate of 0.5 mm/min. The specimens are bolted to the hinges in the same manner as DCB test coupons. The specimens are placed to the fixture as seen in Figure 3.10 with a good horizontal alignment. Moreover, to level the specimen well with the ground a small bubble lever is used on the specimen like in DCB test.

After they are well aligned the displacement is obtained like in DCB test. The displacement is obtained at the tip of the specimens which the hinges are connected to the MMB apparatus as in Figure 3.10. In this experiment the same data receiving fixture is used as on DCB test. So, the triggering is done same with DCB test. Again, as in the DCB test, one sample per second is obtained from both.

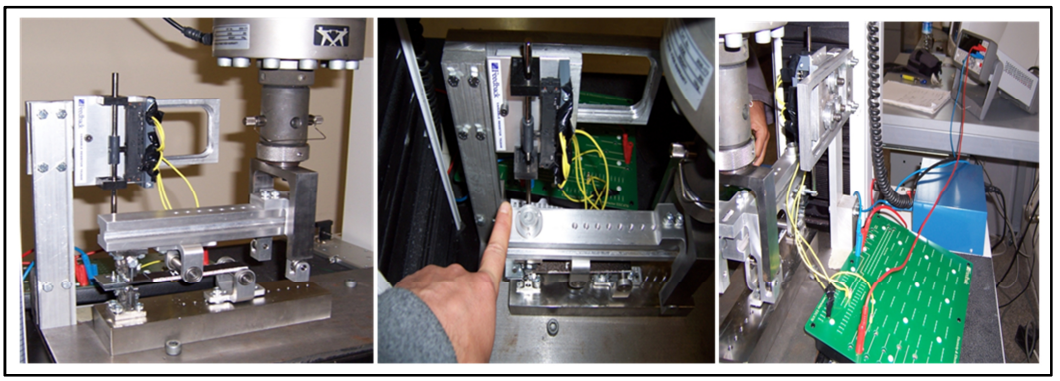

Figure 3.12. Test rig for the MMB test

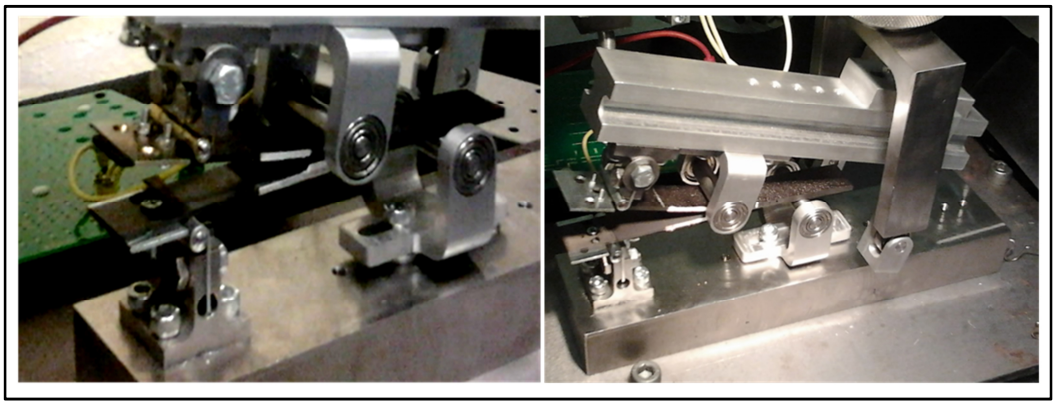

Figure 3.13. MMB test specimen under test.

1.15.4.2. Test Results

For each mode ratio (G_1/G_2) two specimens are used for the MMB tests. The reaction force-displacement curves for the mixed-mode fracture toughness 0.25, 1 and 4 of the specimens are shown in Figure 3.14, Figure 3.15, and Figure 3.16 respectively. The Displacement is the output of the variable resistor and the reaction force is computed by the testing machine.

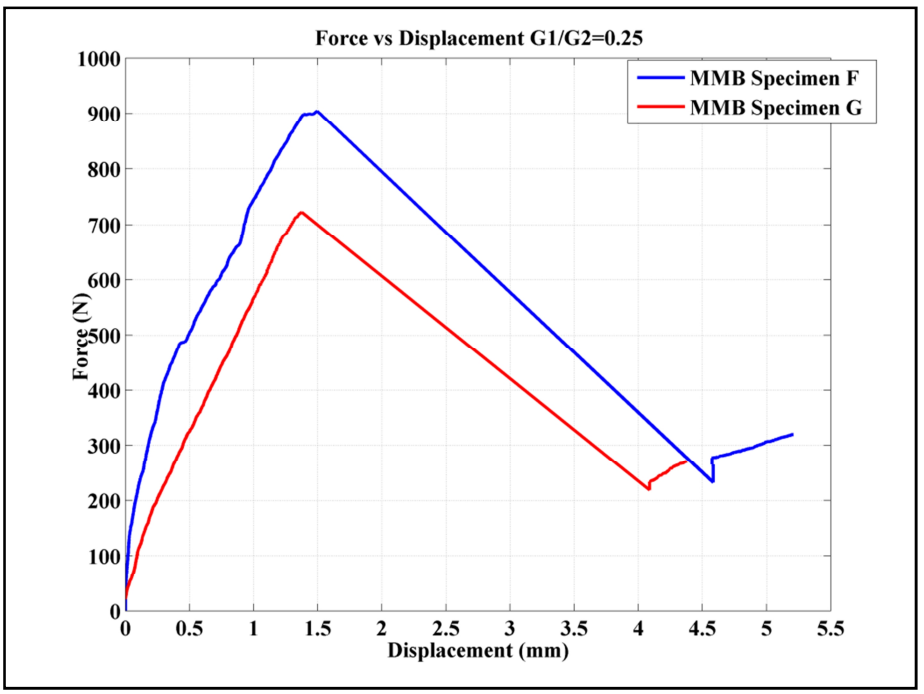

Figure 3.14. The MMB test result for the G_1/G_2=0.25

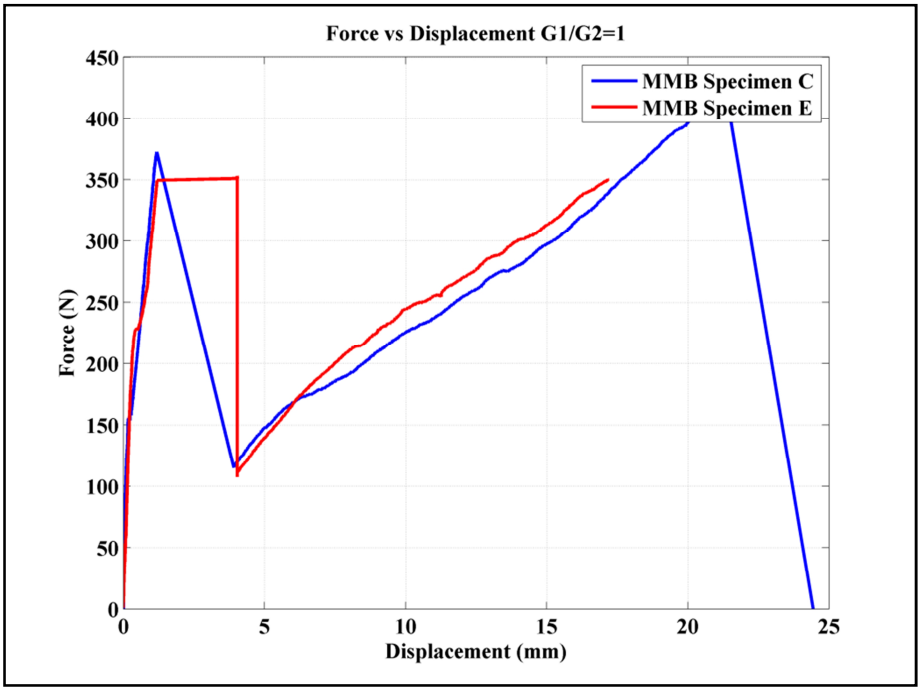

Figure 3.15. The MMB test result for the G_1/G_2=1

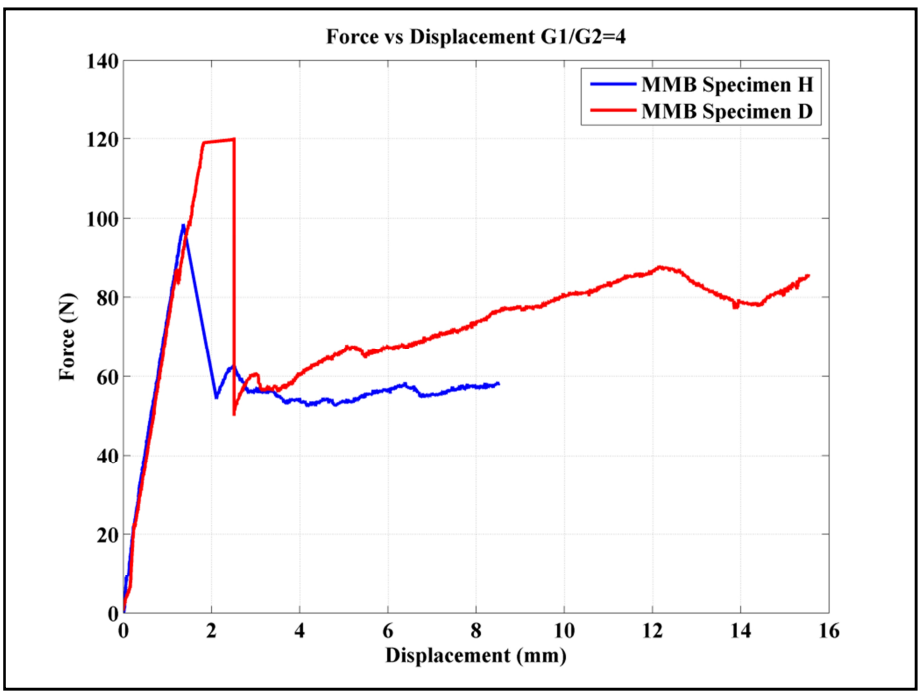

Figure 3.16. The MMB test result for the G_1/G_2=0.25

1.15.5. Overall Static test results

The material properties of the carbon fiber reinforced composite plate used during the static test are given in the tables below. Two critical fracture toughness values are calculated for the mode 1 DCB tests due to the unstable crack growth. The first G_{1c} is calculated based on the first peak of the load-displacement curve of the DCB test and second G_{1c} is calculated based on the second peak on the same plot. For the MMB test, critical G_{1c} and G_{2c} are calculated for each experiment; that is why there are two values for each set of parameters in Table 3.10.

Table 3.9. Material properties (all moduli in GPa and toughnesses in N/mm)

E_{11}	$E_{22} = E_{33}$	E_f	$G_{12} = G_{13} = G_{23}$	$\nu_{12} = \nu_{13}$	ν_{23}	ν_{21}	1^{st} G_{1C}	2^{nd} G_{1C}
154.35	11.46	105.9	3.34	0.32	0.35	0.023	1.20	0.40

Table 3.10. Ultimate tensile strength

Tensile strength 0° (MPa)	1398
Tensile Strength 90° (MPa)	37.07

Table 3.11. MMB test results

G_1/G_2	Pmax (N)	a, crack length	G_1	G_2
0.25	98.56-120.3	39.5-41	0.360-0.340	0.091-0.085
1	351.1-372.5	55.5-57.5	0.330-0.360	0.330-0.360
4	722.3-904.2	58.5-62.5	0.25-0.39	1.00-1.57

1.15.6. Fatigue Test of Tapered Coupons

1.15.6.1. Test procedure

During the tests a hydraulically controlled fatigue machine, Instron 5512, was used at Eskişehir Anadolu University. Loads were applied to the coupons with an R ratio of 0.1, which is a tension to tension profile. In most of the tests, the load magnitude is increased by 10 % after every ten thousand cycles. The load cycles were applied at a frequency of 10

cps. To see the crack growth during the test, specimens are painted white. The crack growth is tried to be followed by a SONY Digital camera. Unfortunately due to the unstable crack growth it is failed to follow the crack growth properly. Because of the lack of measurement of crack growth during the test, some load and displacement graphs and some pictures of the failure of the specimens are illustrated in the result section of the fatigue test.

1.15.6.2. Test Results

For the sample load displacement graphs in every ten thousand cycles, data was captured denser along the beginning of the cycles and along the end of the cycles. Figures 3.18, 3.20 and 3.22 show the graphs of the number of cycles versus number of samples (data points) collected during a fatigue test. As it seems, for the first group of ten thousand cycles, between zero to one hundred cycles, data was captured more densely. Between one hundred and one thousand cycles, the captured data is rarer. Lastly, the cycles between one thousand and nine thousand nine hundred, curve is very steep and very few data points were taken. In Figures 3.18, 3.20 and 3.22, five, five and seven groups of ten thousand cycles formed respectively.

In addition, the data of max-min applied load to the number of cycles of the fatigue tests of the tapered laminates for each configuration given as a table in Appendix B. Figures 3.17, 3.19 and 3.21 show the force vs. displacement cycles for one specimen of each layup configuration, as captured by the fatigue machine. Figures 3.23 and 3.24 show photographs of the failed fatigue specimens and the testing process, respectively.

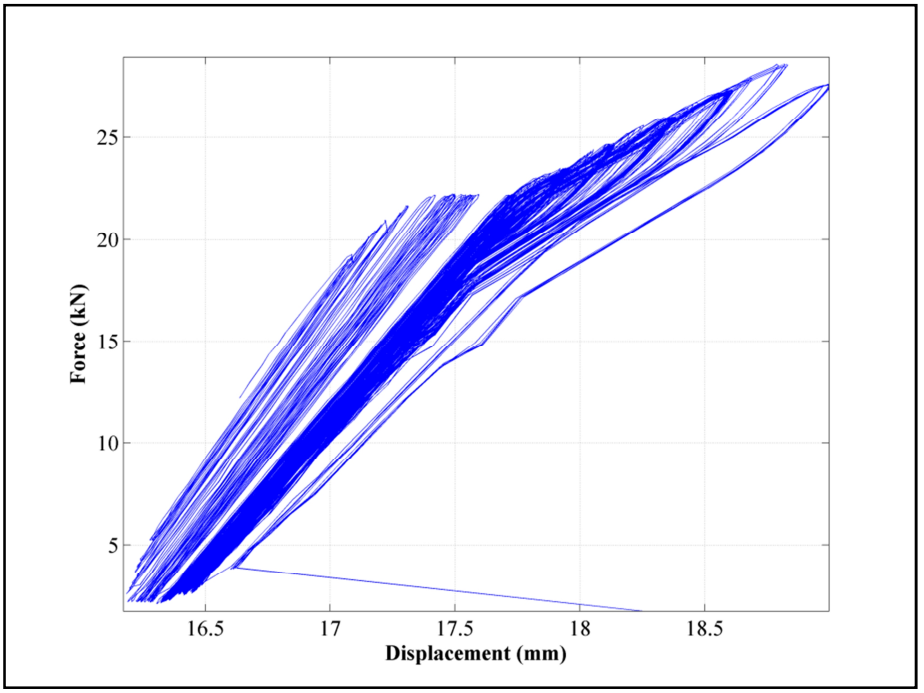

Figure 3.17. The sample load displacement graph for TL1b configuration specimen

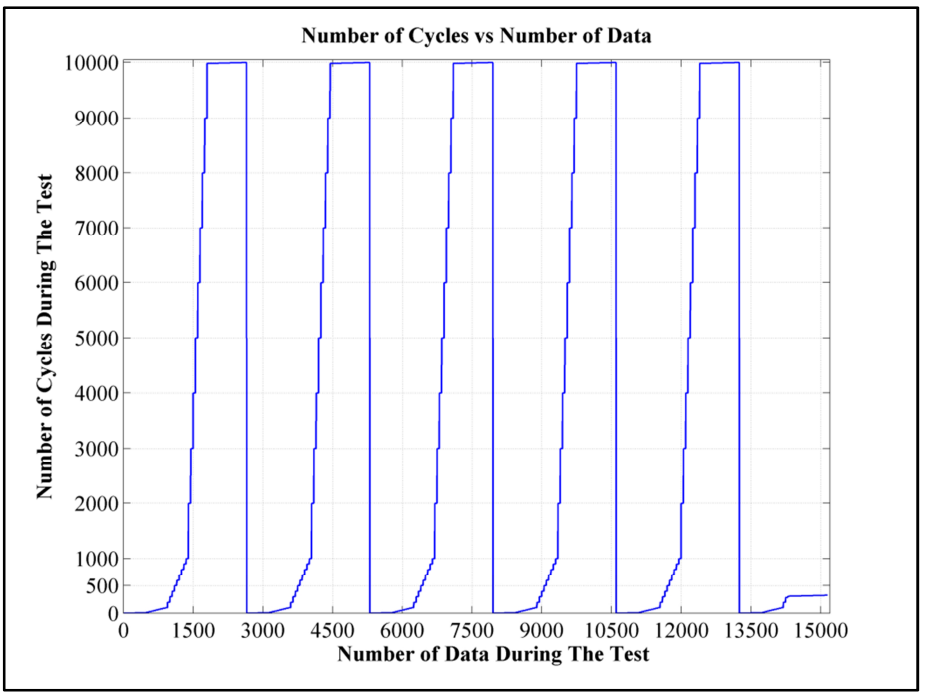

Figure 3.18. Number of cycles vs. number of data graph for TL1b configuration specimen

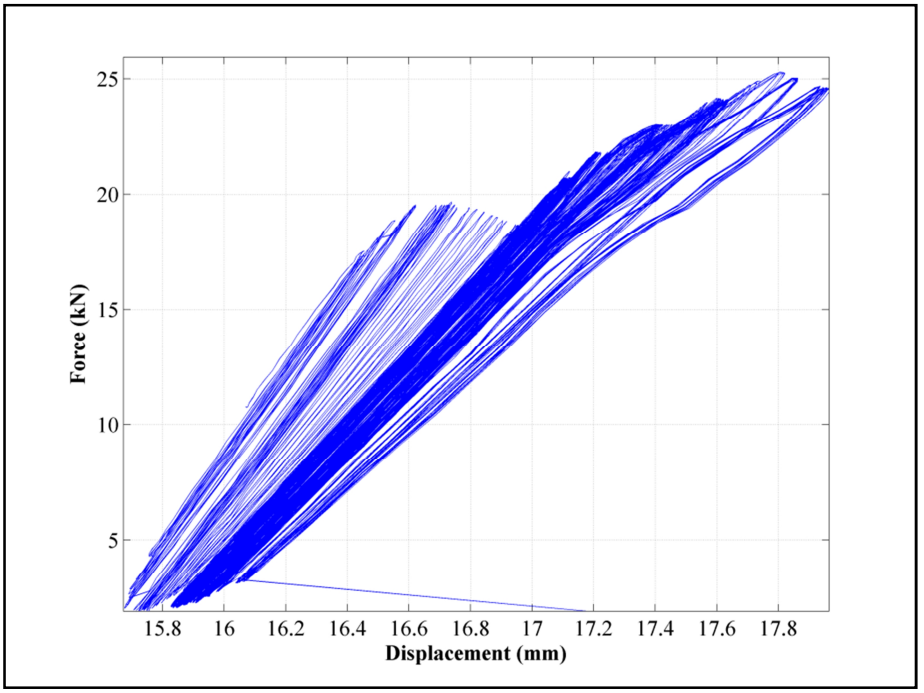

Figure 3.19. The sample load displacement graph for TL2b configuration specimen

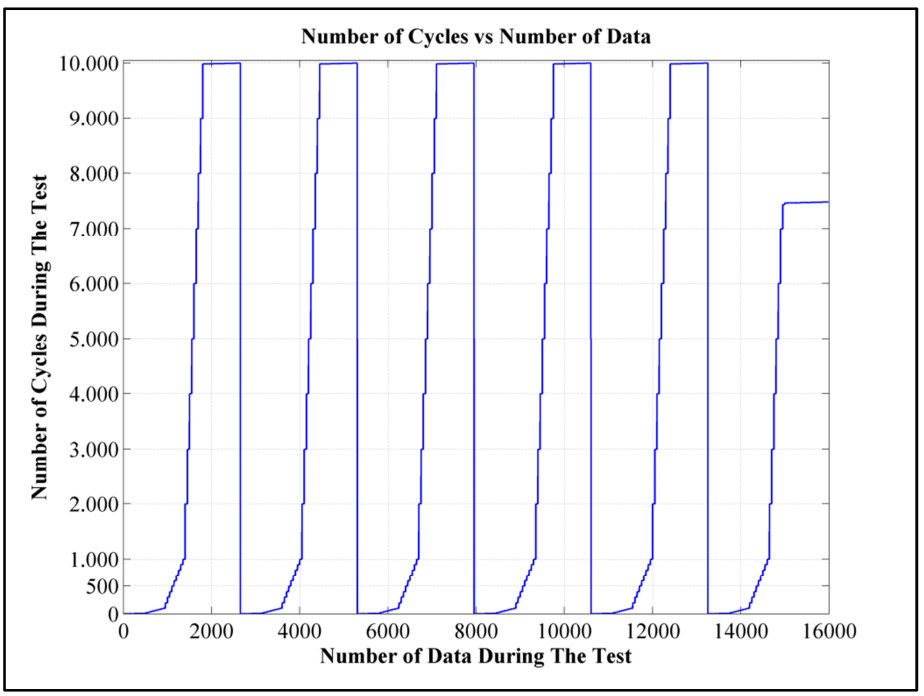

Figure 3.20. Number of cycles vs. number of data graph for TL2b configuration specimen

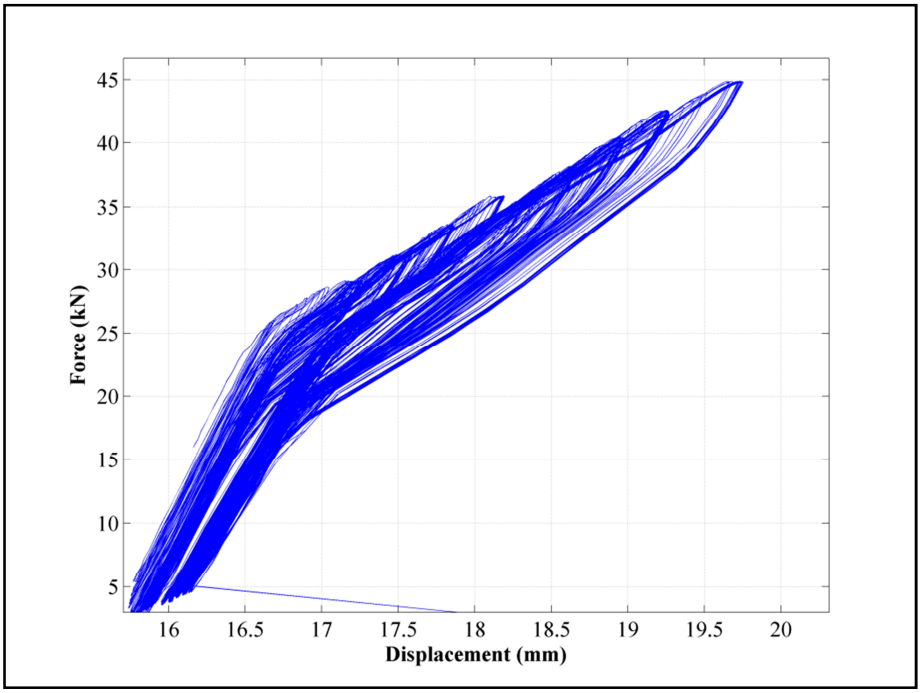

Figure 3.21. The sample load displacement graph for TL3b configuration specimen

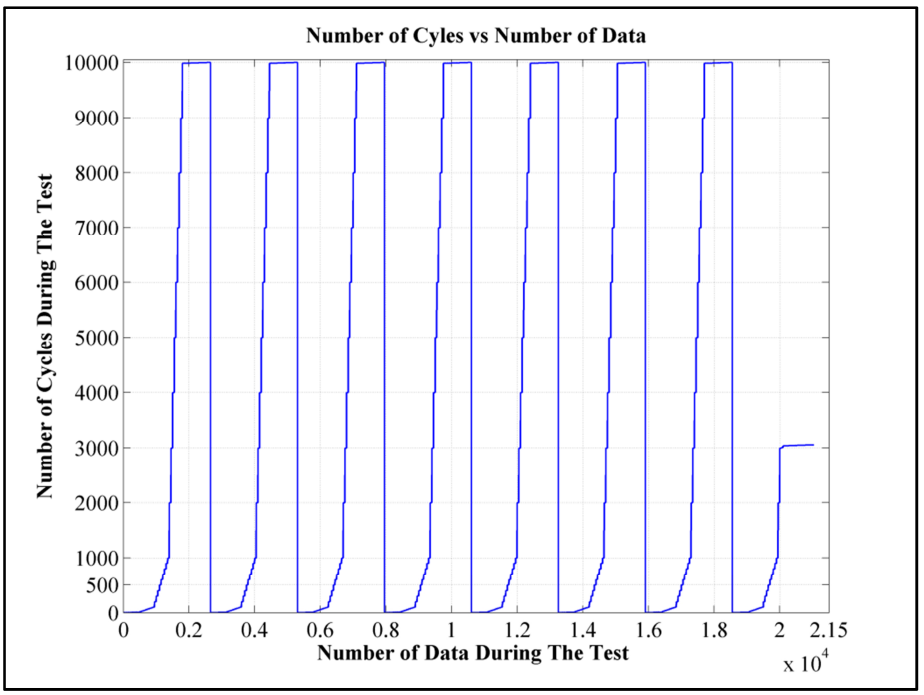

Figure 3.22. Number of cycles vs. number of data graph for TL3b configuration specimen

Figure 3.23. Tested coupons after failure during the fatigue test

Figure 3.24. Some photographs taken during and after the fatigue tests

Close examination of the table in Appendix B leads to the following conclusions:

- There are some discrepancies in the fatigue-life results of specimens in each layup configuration among themselves.

- Specimens of configuration TL3 are the strongest. This is expected since they have the largest number of 0° plies among the three configurations.
- Specimens TL1 have two 0° plies among the dropped ones instead of the two 45° plies in specimens TL2 and would be expected to be stronger than TL2 specimens but the results are rather mixed.
- Specimen TL3b is much stronger than TL3a, that is, lasts a longer time at the same load levels than TL3a. Specimens TL3c and TL3e have very close fatigue strengths. However, despite these differences, specimens of configuration TL3 fail at maximum load levels F_{max} of roughly 42±2 KN independently of the number of cycles and of the load levels at the beginning of each test. The results for the other configurations are more spread.

NUMERICAL STUDY

1.16. INTRODUCTION

Simulation of the delamination process in composite structures is quite complex, and requires advanced FE modeling techniques. In general, failure analysis tools must be able to predict initiation, size and propagation of delamination. This study, however, does not deal with initiation. The presence of an initial delamination is assumed and the growth of the delamination is simulated. The original aim was to simulate growth under fatigue loading. Delamination growth parameters in Paris law were to be determined from fatigue tests. The fatigue tests, however, did not go as planned and it was decided to simulate quasistatic delamination growth by using the fracture toughness results from the DCB and MMB tests. Modeling and simulation studies are described below.

1.17. MODELING

Modeling of DCB has been completed in the following steps.

1. Formation of a model in SOLIDWORKS:
2. Implementation of the model in ANSYS

The model is imported as an input file to ANSYS. Here just the boundary conditions are applied to the model and the VCCT method is applied in ANSYS for delamination analysis to be verified by the test data.

These steps are used to obtain a model which is formed by pure elements and nodes. This process does not create any volume, area, line and so on. This makes it possible to gain flexibility in the activation of the element-kill method to implement the VCCT easily. The implementation of VCCT method is done through APDL (ANSYS Parametric Design Language). By means of APDL the VCCT algorithm is implemented step by step. The analysis is performed in a displacement-controlled manner as in the experiments. Suitable

codes are written through APDL according to the analyses. A sample code can be found in Appendix C.

1.18. VCCT IMPLEMENTATION

VCCT is a useful method for fracture mechanics. Its theory is presented in chapter 2. The VCCT utilizes the product of nodal forces and the difference in nodal displacements to calculate the energy release rate components for each fracture mode. The method is based on the calculation of energy release rate according to two main assumptions [53]:

- Irwin's assumptions that the energy released (ΔE) when the crack is extended from a length of (a + Δa) to (a + 2Δa) (Figure 4.1) is identical to the energy required to close the crack back to (a + Δa), and the forces required to close the crack are identical to the forces acting on the section of length Δa ahead of the crack (a + Δa) prior to its extension to (a + 2Δa).
- A crack extension from (a + Δa) to (a + 2Δa) does not significantly alter the state at the crack tip (self-similar crack propagation). Therefore, the displacements at the current crack tip at node j (Figure 4.1) when the crack extends to length (a + 2Δa) are approximately equal to the displacements at the previous crack tip at node i.

  Mathematically, the work needed to close the crack is given by

$$W = \frac{1}{2} Fu \tag{4.1}$$

  where, according to the assumptions above, F is the force needed to hold together nodes j and j', and u the opening displacement, e.g. the distance between nodes i and i' for an open crack. In Figure 4.1, the force F needed to close the crack virtually can be approximated by the force between Elements 2 and 4 at node j.

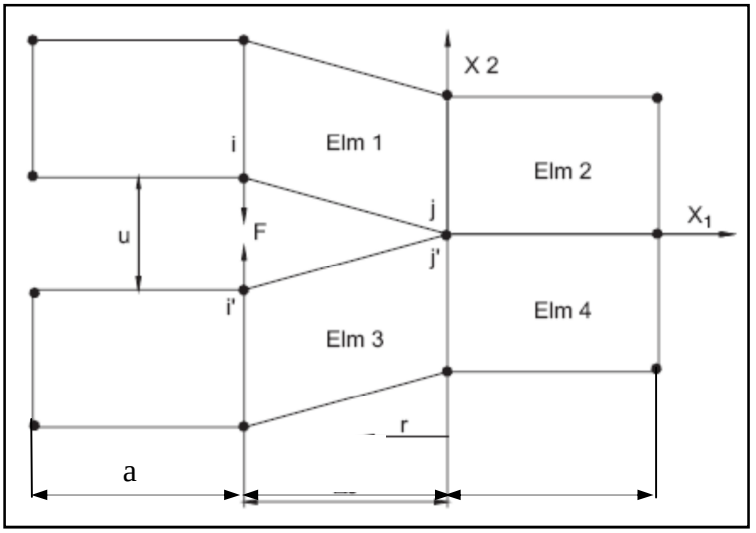

Figure 4.1. 2D finite element model of crack tip closure [54]

The FE procedure of our models is in 3D and the application of the VCCT in 3D FEM models is commonly called the 3D VCCT. The general formulation of 3D VCCT is

——— (4.2)

where G_i is the strain energy release rate, index i controls the direction and index k controls the node number as seen in Figure 4.2.

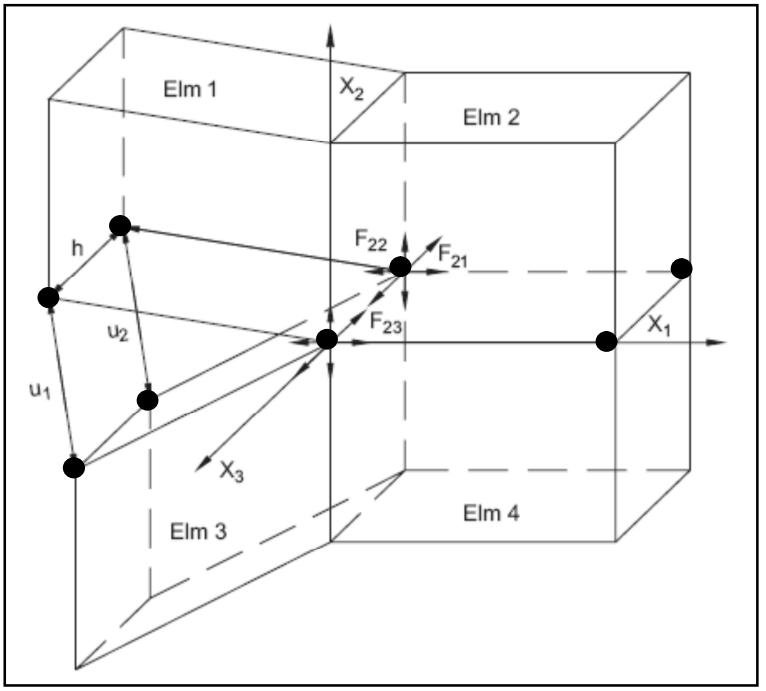

Figure 4.2. The marking for the 3D VCCT [54]

1.19. VERIFICATION ANALYSES

Because of the complicated nature of delamination analysis and of the need to match the simulation results with the experimental ones, it was essential to ensure that the simulation in this study was accurate enough. Toward that end, the results of two studies of delamination growth in a DCB specimen in the literature were verified. These two studies by Alfano and Meo, respectively, have been cited by other researchers 112 times and 10 times, respectively [55]. In addition, the analysis by Alfano is also available as a benchmark solution in several commercial FEM Programs such as ANSYS, ABAQUS etc. In this verification process, models were formed to predict delamination growth by the element-kill approach used in the DCB analysis by Meo and Thieulot [56]. The simulation was done by imposing a tip displacement that increased step-by-step to mimic the displacement-controlled tests. It was assumed that the delamination would grow in between the two centre plies. The interface between the two center composite plies was modeled as an isotropic medium with solid elements representing the matrix (i.e., the resin layer). A solid element at the delamination front was eliminated when its energy release rate exceeded the critical value. The elements were “killed” one at a time. To achieve this,

the ‘Birth and Death’ option provided by ANSYS FE code was utilized. This option can be used to deactivate or reactivate selected elements in certain cases. The ‘killed’ elements were not actually removed but they were deactivated by multiplying their stiffness by a severe reduction factor. Therefore, the complex moving mesh strategy could be handled. The energy release rate was computed using the virtual crack closure technique (VCCT).

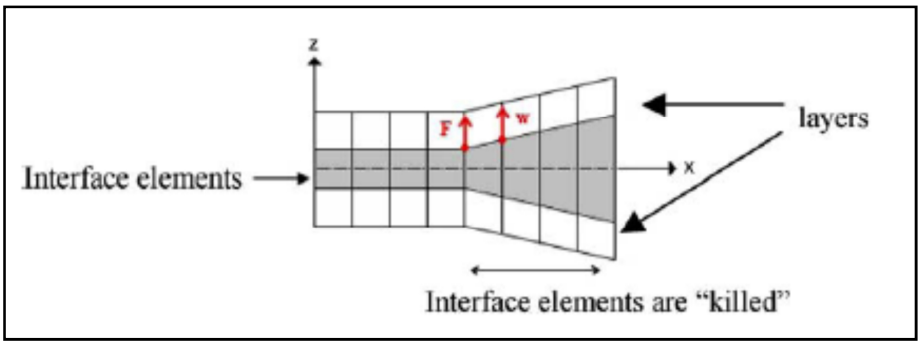

Figure 4.3. Description of the birth and death elements model [53]

In this approach, the researchers seem to prefer to choose the elastic modulus of the interface layer to be the same as the transverse elastic modulus (E_{33} which is E_{zz} in Figure 4.3) of the adjacent plies.

ANSYS requires the nonlinear analysis mode to be selected when a step-by-step analysis is to be performed. At the end of each displacement step, the value of the energy release rate was calculated and compared with the critical energy release rate of the interface (see the description of each simulation below). If the criterion was exceeded, the elements were eliminated. In this analysis only one line of elements (along the width direction) was deleted at each analysis step.

In [53], the analysis of sensitivity to the material properties of the interface showed that the slope of the linear part of the force-displacement curve is dependent on the Young’s modulus of the interface [53].

1.19.1. The simulation of the DCB problem in [53]

The simulation of Meo's problem [53], which is both experimental and numerical, is based on delamination of a DCB specimen of known material properties. In [53], four different ways of modeling delamination growth in a double cantilever beam test (DCB) are proposed, one of which is VCCT where they used a 3D model. In the present 3D study, the verification is based on the VCCT results in [53]. Unfortunately, reference [53] does not contain adequate details. The most important detail missing is the critical strain energy release rate that they used in their simulation. Various questions on the missing details were e-mailed to the authors but a no response was received. In order to estimate a value for their problem, an analysis was initiated with the same initial delamination length as theirs and the tip displacement was increased until the reaction force reached their critical (maximum) value, which is 65 N, at which their specimen began to delaminate. The value of the strain energy release rate at that instant was taken to be the critical value . According to this analysis is computed as . This value is then used as described above. At each step, only the strain energy release rate of the element in the middle of the row of elements at the delamination front is checked against the critical value and, if it is exceeded, the whole row is killed.

The material properties used in [52] are given in Table 4.1. The specimen is 0.185-m long and 0.025-m wide, with two 2.5-mm thick sublaminates, between which a delamination will propagate, and with an initial delamination length of 55 mm. The interface thickness of the model is also 2.5 mm as given in [53] and used here. The DCB test specimen in the study is a 24-ply UD laminate ( ) made from a carbon-fiber-reinforced polyetheretherketone (C/PEEK). The specimen geometry is given in Figure 4.4.

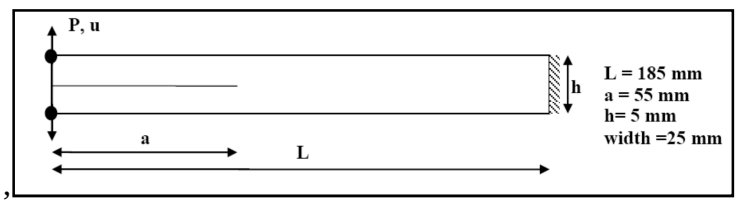

Figure 4.4. DCB geometry in [53]

In the present simulation, the specimen was built with 64, 7 and 3 elements along the x, y and z directions, respectively. The FE model was built with 1344 8-noded elements. For the element type, solid 45 and solid 46 type elements were chosen. Solid 45 was used for the interface and Solid 46 was used for each of the two composite sublaminates. The first 19 rows of 7 elements each, starting from the specimen tip at the interface were killed initially to simulate the initial delamination. The nodal degrees of freedom (DOF) in all three directions at the support were fixed. Initial number of DOF of the system before any elements were killed was 6032. In Figure 4.5, the boundary conditions at the support and the reaction forces at the tip are also depicted. In Figure 4.5, the parameters u v and w are the displacements to the x y and z directions respectively.

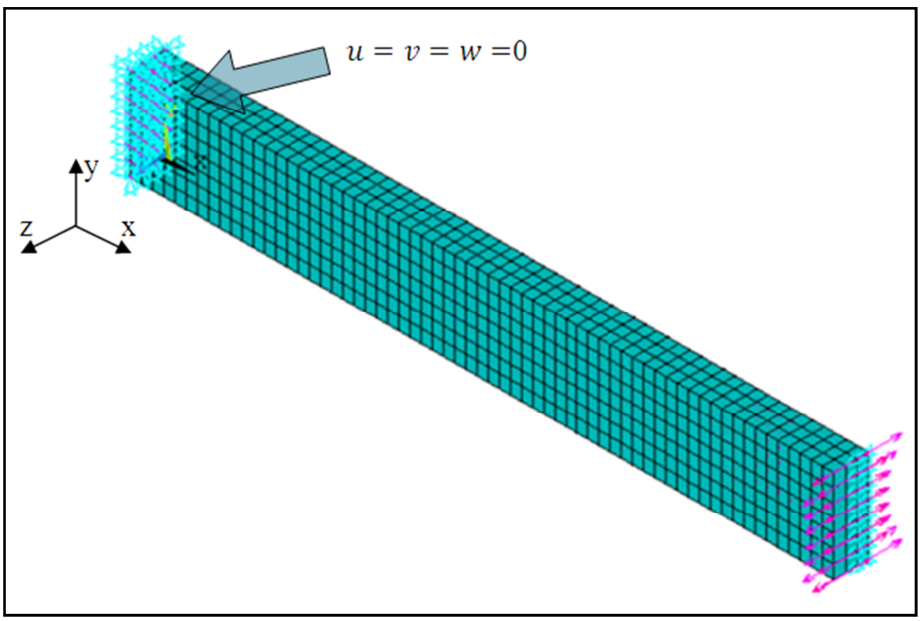

Figure 4.5. The boundary conditions and the force reactions in the present ANSYS model of the work in [53]

Table 4.1. Material Properties for APC-2 / AS4-CFRP Used in [53]

135 GPa	9 GPa	5.2 GPa	1.9 GPa	0.34	0.46

The present simulation used 40 steps as was the case in [53]. The plot in Figure 4.6 shows the finite element and experimental results in [53] and the FE results here. All three

curves are in quite good agreement. The adopted modeling approach was clearly capable of describing the delamination behavior.

1.19.1.1. Comparison of Results

The comparison of the result of the modeling technique with experimental data showed that very good correlation was achieved. The Table 4.2 shows that the errors between the results in each analysis.

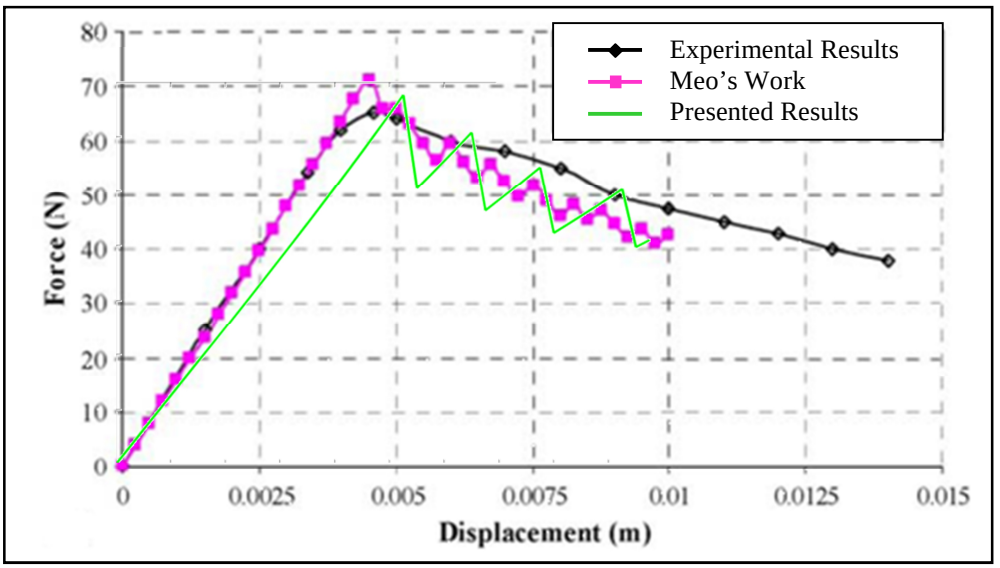

Figure 4.6. The load point displacement vs. Force in simulation of Meo's work and presented work with experiment

Table 4.2. Tapered Specimens Dimensions

	Experimental Results	**Meo's Work Results**	**Presented Simulation Results**	**% Error Between Meo's st. & Presented**	**% Error Betw. Exp. Data & Presented**
Force (N)	65.000	72.000	60.700	15.694	6.610
Disp. (mm)	4.600	4.600	4.600	4.600	4.600

1.19.2. The simulation of the DCB problem in [56]

In the work of Alfano and Crisfield [56], again a pure mode 1 problem, a double cantilever beam was analyzed under displacement control. They simulated an experimental study reported in the literature as a 2D problem. They used two methods in their simulation, namely, cohesive zone elements (CZM) and the VCCT and compared them. They probably used a multi-point constraint (MPC) facility that exists in many FE codes to separate the nodes at the delamination front as the delamination propagates. Their geometry is described in Figure 4.7 and the material data are given in Table 4.3. A regular mesh of 4x400 eight-node plane strain elements and 280 six-node interface elements was used in [56]. The specimen is 100-mm long and 20-mm wide, with two 1.5-mm thick sublaminates and with an initial delamination length of 30 mm. The interface thickness of the model is 0.75 mm. Their results are shown as load-point-displacement vs. reaction-force plots in Figure 4.9.

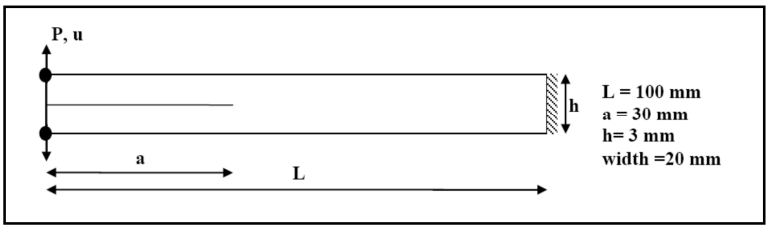

Figure 4.7. DCB geometry in [56]

Table 4.3. Material Properties Used in [56]

135.3 GPa	9 GPa	5.2 GPa	5.2GPa	0.24	0.46	0.28 N/mm

The reason for simulating a second DCB problem from the literature is the difference between the approaches in [53] and [56]. It was desired two check the present modeling effort against a 3D analysis with the VCCT [53] and the element-kill approach, a 2D analysis with the VCCT coupled with MPC facility and a 2D analysis with the CZM [56]. For the verification of the analyses in [56], a FE model was built in the same geometry as in [56].

Along the x, y, z directions the specimen was built with 64, 1, 3 elements, respectively. The FE model used 150 8-noded Solid 185 type elements for the whole specimen. This special type of element has the capability of enhanced strain to overcome hourglass effect on bending due to large displacements. The first 15x1 elements starting from the specimen tip at the interface were killed initially as the initial delamination. The nodal degrees of freedom (DOF) in all three directions at the support were fixed. The number of DOFs of the system before any elements were killed was 1208.

In Figure 4.8, the boundary conditions are depicted. The parameters u v and w are the displacements to the x y and z directions respectively.

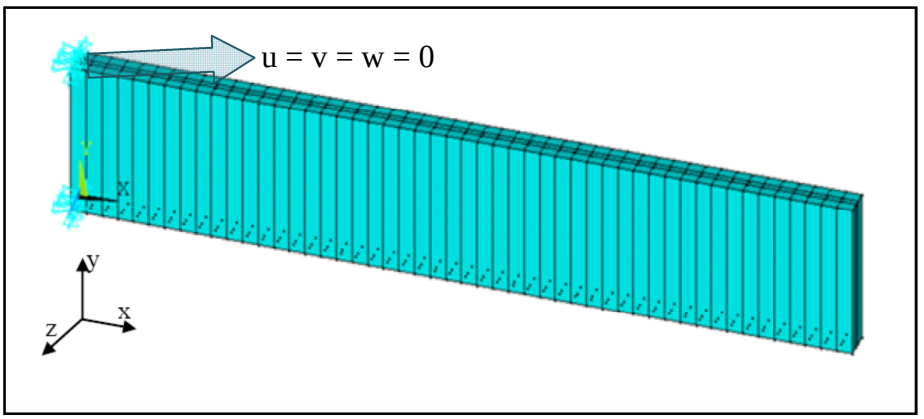

Figure 4.8. Boundary conditions for the presented solution

This problem is similar to the problem in [53] with different type of materials and different dimensions. The problem was solved in 159 steps. Unlike the study in [53], the critical strain energy release rate was given in [56]. Hence an element-kill model of the problem was built with a different value of , different dimensions and with a different of element mesh.

1.19.2.1. Comparison of Results

The comparison of the present numerical results with those in [56] shows a very good correlation. In figure 4.10, the out of plane stresses which are the causes for the delamination are shown too.

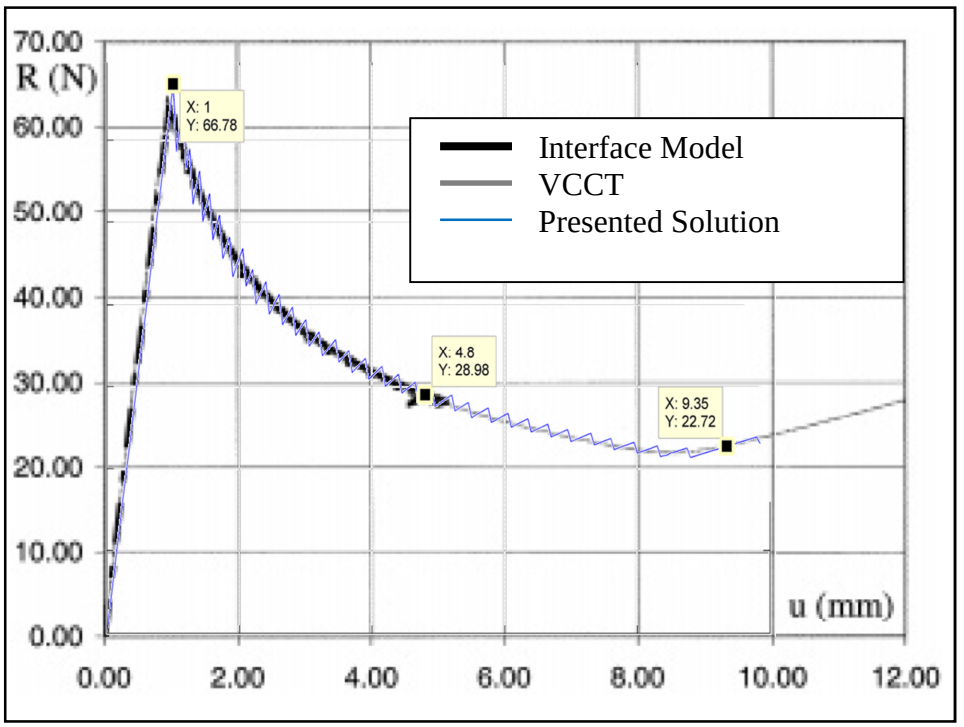

Figure 4.9. Load-point-displacement vs. reaction-force

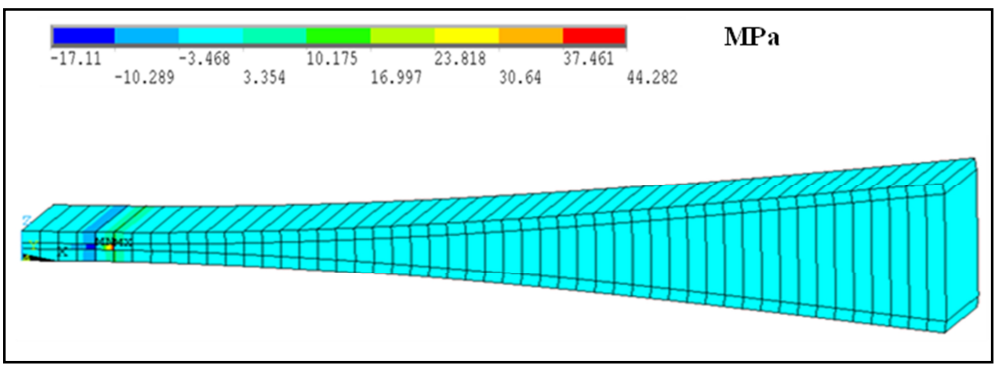

Figure 4.10. Normal stress distributions at the crack tip at the end of the analysis

1.19.3. Simulation and Verification of the Present Experimental Study

In this section, the results of the simulation of the DCB experiments conducted in the present study will be presented with the same procedure used for verifying the works in [53, 56]. The parameter values used for the verification are based on the DCB experiments of this study.

The physical specimen, made of 28 UD plies (0_{28}), was 157-mm long, 20-mm wide and 4.4-mm thick. The dimensions of the specimen are given in Figure 4.11. In the FE model, the interface thickness was taken as 0.6 mm. The sublaminates on each side of the delamination plane, each 2.2 mm thick, are modeled with 2 elements through the thickness. Total thickness of the 3D simulation model is 5.0 mm with a total of 5 elements through the thickness. The material properties of the specimen are given in Table 4.4.

It was assumed that the delamination would grow symmetrically with respect to the transverse symmetry plane, even though this was not exactly the case for some specimens in the tests, and a half FE model was generated as seen in Figure 4.12. The half model was built with 143, 1, 5 elements along the x, y, z directions, respectively. The FE model is built with 429 8-noded Solid 185 type elements which were used for the whole specimen. The first 35x1 elements starting from the specimen tip at the interface were killed initially as the initial delamination. The DOFs in the x and y directions at the tip nodes where a step-by-step displacement is applied in the z direction were fixed. In addition, on whole symmetry plane the y displacements were fixed. The number of DOFs of the system before any elements were killed is 7054.

Figure 3.11 shows the force-displacement curve obtained experimentally. As seen there is a sudden drop of 96 N at a load-point-displacement of 1.7 mm. (It is noted that, in the test, the bottom hinge on the specimen is kept fixed and the upper jaw of the machine moves up. The displacement of 1.7 mm in the figure is the displacement of the upper hinge whereas in the FE model half of this would be applied to the upper sublaminate and half to the lower one in the opposite direction.) This sudden drop did not exist in References [53, 56]. It is believed that this is due to the use of a $200\,\mu m$ thick teflon film in laminate production, to create an initial delamination. A $13\mu m$ thick film, as suggested in ASTM

5528 DCB test standard [57], should have been used instead. Initial crack growth was therefore unstable.

In order to cope with this problem two G_c values were calculated from the experimental plot, based on simple beam theory equation 2.8 to simulate the DCB experiment. The values were 1.2 N/mm and 0.4 N/mm before the initial delamination extension and for the propagation afterwards, respectively. The second G_c value is used beyond 1.7 mm of displacement. The APDL code used is modified to handle this situation. In order to simulate the force drop of 96 N, when the strain energy release rate in the element at the delamination front reaches the first critical value of 1.2 N/mm, the code kills that element and, without yet increasing the displacement to the next step, continues to check the other elements at the front, killing them one by one if their energy release rate is above the critical value also. This continues until an element is reached with less than the critical energy release rate. With this approach, 11 elements were killed before incrementing the displacement to the next step. After the first 11 elements, the second critical value =0.4 N/mm was used. The analysis was completed in 159 steps.

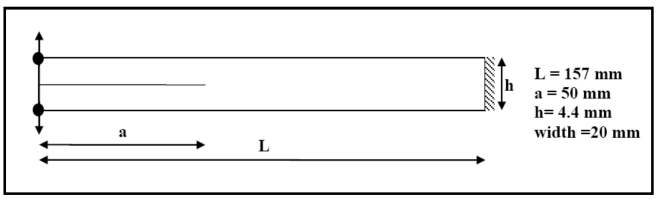

Figure 4.11. DCB geometry for the presented study

Table 4.4. Material properties for the presented study

154.35 GPa	11.46 GPa	3.34 GPa	0.32	0.35	1.20 N/mm	0.40 N/mm

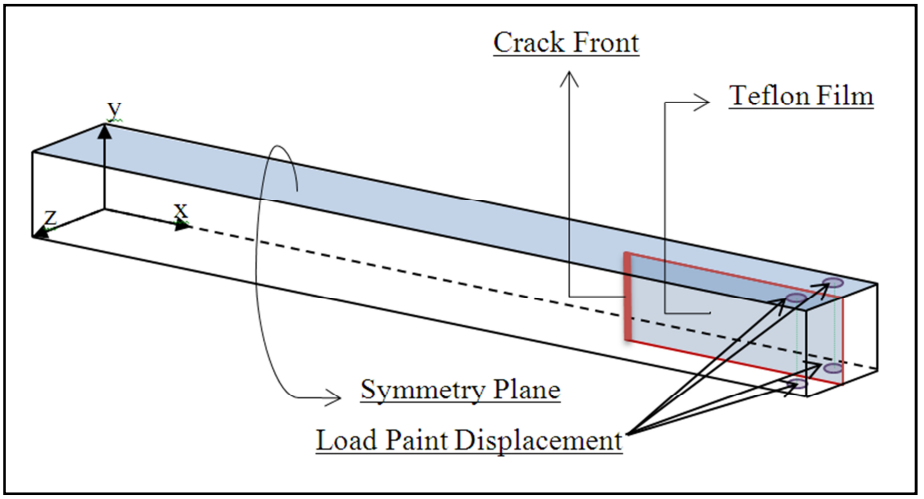

Figure 4.12. Half model for the presented simulation

1.19.3.1. Comparison of Results

The comparison of the result of the modeling technique with the experimental study showed that quite good correlation was achieved. There is 12.74 % and 2.15 % error between the results for displacement and force, respectively, at the first peak of the resulted plot in Figure 4.14. In Figure 4.13, the out of planes stresses which are the reason for the delamination are shown too.

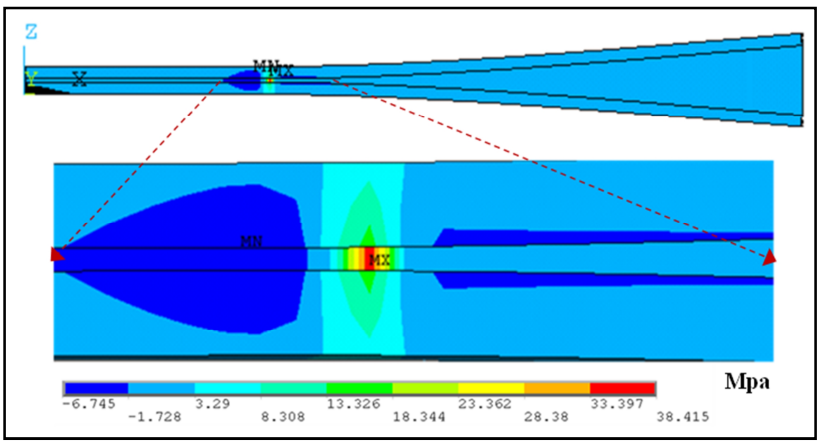

Figure 4.13. Normal stress distributions at the crack tip at the end of the analysis

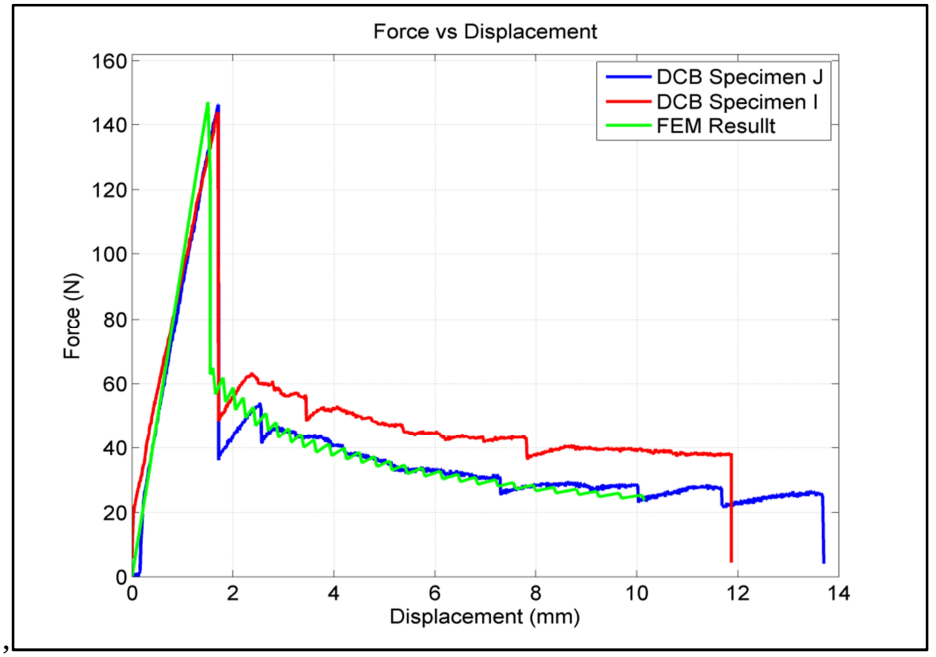

Figure 4.14. Simulation result with experimental data

CONCLUSIONS

In this study, delamination growth in a double cantilever beam (DCB) specimen, which is used to measure critical strain energy release rate under a mode I type of loading, was investigated experimentally and numerically. In addition, delamination growth in mixed mode beam (MMB) specimens were tested to measure critical strain energy release rates under mixed mode I and mode II types of loading and fatigue tests were conducted on tapered laminates. The material in all cases was carbon fiber reinforced epoxy. Delamination growth was simulated with a fracture mechanics approach (VCCT). Simple tension tests and three point bending tests were conducted as well to determine basic material properties.

In order to implement the VCCT method element–killing strategy was used. This method provided a solution to handle moving meshes during crack propagation.

As a result, based on this study the conclusions can be divided into two parts as experimental and numerical.

1.20. CONCLUSIONS FROM THE EXPERIMENTAL STUDY

Several types of experiments were performed. These are tension tests, three point bending tests, DCB tests, MMB tests and fatigue tests. The conclusions are listed below:

- Reliability of the tension tests were proven with the ratios of E_{11}/ν_{12} and E_{22}/ν_{21} obtained from the 0° and 90° tests. The error between these ratios was very low (an error of 3.3 %).
- The thickness of the teflon insert in a DCB/MMB specimen is very important. The teflon which is used to produce the initial delaminations between the mid layers was 200 µm. On the other hand the suggested film thickness is 13 µm [57]. This produced a big handicap for determination of G_c. The thick teflon film made the DCB/MMB samples to require more energy to be released for delamination growth. The initial delamination growth was unstable instead of gradual because of the high strain-energy build-up and a fairly large growth increment occurred. It also changed

the compliance of the specimen for the subsequent growth. Therefore, different values of G_c were obtained for the initial and subsequent growths. During the subsequent growth period, there were small but unstable growths followed by some stable growth which would again be followed by a sudden small delamination jump. The obtained experimental data could not be correlated with the data reduction method in the relevant standard [57]. The standard suggested three ways of determination of critical G_c value. The suggested methods were tried but according to the found critical values, the numerical simulations could not be correlated with the experimental data. Instead of using these methods the simple beam theory was used for the determination of the G_c and good correlation was obtained with the numerical results.

- Attaching the hinges to the specimens requires care. Initially the hinges for transferring the loads from the clamps of the test machine to the tip of the specimen where the initial delamination is located were bonded by cyanocacrylate (superglue). Unfortunately this kind of bonding failed due to the high load resistance of the specimens. Because of the reason of this failure instead of using bonded hinges the hinges were attached to the specimens mechanically.
- Observation and recording of the amount of delamination growth, especially in MMB tests, is an important part of these tests. The sides of the coupons were painted white and marked with pencil to visualize crack growth. However it was very hard to maintain a correct marking and the apparatus itself was partly blocking the view as the delamination approached the intermediate roller location. As a result, there should be suggested a way of marking to provide more accurate and simple marking process. In addition, to follow the crack growth it is essential to have a travelling microscope to determine the precise crack lengths.
- The alignment of the specimen between the lever and the base of the MMB apparatus needs an intense care to eliminate rotation of the lever about its own axis. It was quite difficult to handle the alignment of the apparatus and the test specimen.
- The test area must be well lit for clear visibility of the specimen and crack growth.
- Fatigue tests were conducted on tapered specimens but the tests were a disappointment. The initial crack growth occurred unstably by a large amount of energy release. No stable growth was observed in any specimen and therefore no

data were available to extract Paris law parameters. The reason(s) for this behavior is(are) unknown.

1.21. CONCLUSIONS FROM THE NUMERICAL STUDY

Due to the lack of fatigue test results, it was not possible to simulate the propagation of fatigue delamination growth. Only the DCB test simulations could be verified by means of linearly elastic fracture mechanics approach “VCCT”. Good correlation was obtained between DCB experiments and simulations.

The element kill method was applied to the MMB specimens to verify the corresponding test results but the approach did not work in this study for delamination growth modes other than mode 1. The interface elements between the upper and lower sublaminates of a specimen have a definite thickness which influences the numerical bending behavior of a MMB specimen by way of increasing the area moment of inertia. This thickness has negligible influence on numerical behavior of a DCB specimen. An interface element with zero thickness should be used in MMB modeling, which can be done with a code that has multi-point constraint (MPC) facility. MPC is required to separate the nodes of a zero-thickness element to simulate delamination.

APPENDIX A: COMPARISON OF VCCT AND COHESIVE ZONE METHOD

The table below shows the advantages and disadvantages of two approaches used for delamination growth simulation.

Table A.1. Comparison of VCCT and cohesive elements [58]

VCCT	Cohesive Zone Method
• Simulation (mechanics)-driven crack propagation along a known crack surface.	• Simulation (mechanics)-driven crack propagation along a known crack surface. However, cohesive elements can also be placed between element faces as a mechanism for allowing individual elements to separate.
• Models brittle fracture using LEFM only.	• Models brittle or ductile fracture for LEFM or EPFM. Very general interaction modeling capability is possible.
• Uses the debond framework. Does not require additional elements.	• Requires definition of the connectivity and interconnectivity of cohesive elements with the rest of the structure. For accuracy, the mesh of cohesive elements may need to be smaller than the surrounding structural mesh and the associated “cohesive zone.” As a result, cohesive elements may be more expensive.
• Requires a pre-existing flaw at the beginning of the crack surface. Cannot model crack initiation from a surface that is not already cracked.	• Can model crack initiation from initially uncracked surfaces. The crack initiates when the cohesive traction stress exceeds a critical value.

Table A.1. Comparison of VCCT and cohesive elements [57] (continue)

VCCT	Cohesive Zone Method
• Crack propagates when strain energy release rate exceeds fracture toughness.	• Crack propagates according to cohesive damage model, usually calibrated so that the energy released when the crack is fully open equals the critical strain energy release rate.
• Multiple crack fronts/surfaces can be included.	• Multiple crack fronts/surfaces can be included.
• Crack surfaces are rigidly bonded when uncracked.	• Crack surfaces are joined elastically when uncracked.
• Requires user-specified fracture toughness of the bond.	• Requires user-specified critical traction value and fracture toughness of the bond, as well as elasticity of the bonded surface.

APPENDIX B: DATA OF APPLIED MAX. AND MIN. LOAD TO THE NUMBER OF CYCLES OF THE FATIGUE TESTS OF THE TAPERED LAMINATES

The Table B.1 shows the number of cycles corresponding to the minimum load and maximum load during the fatigue tests of the tapered specimens for each configurations.

Table B.1. Data of Max-Min force to the number of cycles of the fatigue tests of the tapered laminates (the last number in the “Cycles” column for each specimen denotes the fatigue life)

Configuration	Cycles	Max Load (kN)	Min Load (kN)
TL 1a	1-10000	22.2	2.2
	10001-20000	23.5	2.32
	20001-30000	24.7	2.5
	30001-40000	26	2.6
	40001-50000	27.1	2.8
	50001-60000	28.5	3.1
	60001-63182	29.6	3.35
TL 1b	1-10000	22.2	2.2
	10001-20000	23.5	2.32
	20001-30000	24.6	2.5
	30001-40000	26	2.6
	40001-50000	27.2	2.8
	50001-50324	28.6	3.1
TL 1c	1-29898	22.3	2.2
	29899-39890	23.5	2.32
	39891-49906	24.7	2.5
TL 1d	1-3	19.74	7.82
	4-6	20.94	6.36

Table B.1. Data of Max-Min force to the number of cycles of the fatigue tests of the tapered laminates (the last number in the “Cycles” column for each specimen denotes the fatigue life) (continue)

Configuration	Cycles	Max Load (kN)	Min Load (kN)
TL 1d	7-9	22.79	4.11
	10	23.04	3.26
	20	24.47	2.52
TL 1e	1-10000	22.2	2.22
	10001-20000	23.5	2.35
	20001-30000	24.6	2.46
	30001-31601	26	2.6
TL 1f	1-112260	15	1.5
	112261-136273	16.5	1.65
	136274-159947	18.2	1.82
	159948-193862	20.7	2.07
	193863-245662	25.6	2.56
	245663-252409	26.7	2.67
TL 2a	1-5000	19.5	1.95
	5001-10000	18.7	2.8
	10001-20000	19.9	2.9
	20001-30000	21.8	2.2
	30001-40000	23	2.3
	40001-50000	24.2	2.4
	50001-60000	25.3	2.5
	60001-70000	27.6	2.9
	70001-71554	28.6	3
TL 2b	1-5000	19.5	1.95

Table B.1. Data of Max-Min force to the number of cycles of the fatigue tests of the tapered laminates (the last number in the “Cycles” column for each specimen denotes the fatigue life) (continue)

Configuration	Cycles	Max Load (kN)	Min Load (kN)
TL 2b	5001-10000	18.5	2.85
	10001-20000	20.7	2.1
	20001-30000	21.8	2.2
	30001-40000	23	2.3
	40001-50000	24.1	2.4
	50001-57485	24.6	2.5
TL 2c	1-5000	19.6	1.95
	5001-10000	18.7	2.8
	10001-20000	20.7	2.1
	20001-30000	21.8	2.2
	30001-31616	23	2.3
TL 2d	1-10000	21.6	2.45
	10001-20000	23	2.3
	20001-30000	24.2	2.4
	30001-40000	25.25	2.6
	40001-50000	25.1	4
	50001-60000	27.5	3
	60001-70000	28.6	3.1
	70001-70142	29.4	4
TL 2e	1-10000	20.8	3.2
	10001-20000	22	3.4
	20001-40000	25.25	2.6
	40001-50000	24.2	4.8
	50001-60000	27.6	2.8
	60001-70000	42.4	4.5
	70001-80000	28.7	3

Table B.1. Data of Max-Min force to the number of cycles of the fatigue tests of the tapered laminates (the last number in the “Cycles” column for each specimen denotes the fatigue life) (continue)

Configuration	Cycles	Max Load (kN)	Min Load (kN)
TL 2e	80001-82048	29.8	3.2
TL 3a	1-10000	33.6	3.4
	10001-20000	35.8	3.6
	20001-30000	38.2	4
	30001-40000	40.2	4.4
	40001-40141	42.6	4.4
TL 3b	1-10000	29	2.9
	10001-20000	31.4	3.2
	20001-30000	33.6	3.5
	30001-40000	35.8	3.7
	40001-50000	38.2	3.9
	50001-60000	40.4	4.2
	60001-70000	42.6	4.4
	70001-73059	44.9	4.6
TL 3c	1-10000	38.15	4
	10001-20000	40.4	4.05
	20001-20296	42.6	4.4
TL 3d	1-10000	33.6	3.4
	10001-20000	35.8	3.7
	20001-30000	38.1	4
	30001-30507	40.3	4.1
TL 3e	1-10000	38.15	3.8
	10001-20000	40.4	4.1
	20001-20144	42.6	4.3

APPENDIX C: SAMPLE CODE FOR APDL

The code shown below is a sample code for the solution phase of the DCB experiment. Similar codes were written for verification of Meo's [53] and Alfano's [56] work.

Algorithm C.1. Sample code for APDL

```
!!!!!!!!!!SOLUTION PHASE OF DCB EXPERIMENT

K1=1
K2=2



*dim,Resfd,,450
*dim,resff2,,450 !1st
*dim,Resfd2,,450

*dim,G,,450

*dim,ResF,,450
*dim,resff,,450


*dim,RFz1,,450
*dim,RFZ2,,450
*dim,W1,,450
*dim,W2,,450


*dim,NW1,,450
*dim,Nw2,,450
*dim,NRFZ1,,450
*dim,NRFZ2,,450

*dim,E1,,36


```

```
32
33
34
35 Ex1=108
36 Ex2=551
37 Ex3=550
38
39
40 *do,ni,1,35,1
41
42 E1(ni)=Ex1                !cracktip element
43
44 NW2(ni)=Ex2                      !cracktipdisplacement node
45
46 NRFZ2(ni)=Ex3                    !Cracktip force node
47
48
49 Ex1=Ex1-1
50
51 Ex2=Ex2-1
52
53 Ex3=Ex3-1
54
55
56
57
58 *enddo
59
60
61 *dim,ff11(X),,450
62 *dim,ff12(X),,450
63
64
65 *dim,ff15(X),,450
66 *dim,ff16(X),,450
67
68
69 /solu
70
71
72 *dim,displacementy,table,2,1     !force table
73 *dim,idisplacementy,table,2,1
74
75 displacementy(1,1)=0,10  !displacement values in column 1
```

```
displacementy(1,0)=0,100
displacementy(0,1)=1

idisplacementy(1,1)=0,-10       !displacement values in
column 1
idisplacementy(1,0)=0,100
idisplacementy(0,1)=1           !2nd


TM_START=1E-6                   ! Starting time (must be >
0)
TM_END=20                       ! Ending time of the
transient
TM_INCR=1                       ! Time increment

                                !*dim,UX55,array,5 !
Create array parameter

NLGEOM,ON                       ! Turns large-deflection
effects on
NROPT,FULL                ! You must explicitly set the
Newtn-Raphson opt.
ekill,BEGIN               !3rd

                                !*dim,comm,char,1
                                !comm(1)='csf'
                                !aa=1

                                !DELTIM,1,0,0

                                !outres,basic,4
                                !outpr,all,all

X=1
*DO,TM,TM_START,TM_END,TM_INCR       ! Do for TM from
TM_START to TM_END in
                                     !4th
/solu


                                     ! steps of TM_INCR

TIME,TM                              ! Time value
113                             ! Time-varying force !5th
```

```
D,312, UZ, displacementy(TM), ,312
D,147, UZ, displacementy(TM), ,147

D,573, UZ, idisplacementy(TM), , 573
D,170, UZ, idisplacementy(TM), , 170

*IF,K1,LT,2,THEN

*IF,G(X-1),GE,.660,THEN        !6th

EKILL,E1(K1)
K1=K1+1
K2=K2+1

ival=1
eval=40
*do,op,ival,eval
/solu
TIME,TM ! Time value
D,312, UZ, displacementy(TM), ,312
D,147, UZ, displacementy(TM), ,147

D,573, UZ, idisplacementy(TM), , 573
D,170, UZ, idisplacementy(TM), , 170


*IF,G(X-1),GE,.2,THEN                !6th
EKILL,E1(K1)
K1=K1+1
K2=K2+1

*elseif,G(X-1),LT,.2
*exit
*enddo
*endif
SOLVE                                ! Initiate solution
calculations
finish

/post1
*GET,W2(X), node,NW2(K1), U,Z
*GET,resfd(X), node,312, U,Z
```

```
156 *GET,ff11(X), node,312, RF,FZ
157 *GET,ff12(X), node,147, RF,FZ  ! REACTION FORCE AT TIPS
158
159 *GET,ff15(X), node,573, RF,FZ
160 *GET,ff16(X), node,170, RF,FZ
161
162 *GET,resfd2(X), node,573, U,Z
163
164 a=ff11(x)+ff12(x)
165
166
167
168 resff2(X)=a
169
170 /post26
171 esol,2,E1(K1),NRFZ2(K1),F,Z,NF1
172 vget,RFz1(X),2,X               ! Store time history data
of variables
173
174 finish
175
176 G(X)=(-1*2*RFz1(x)*W2(X))/40
177 X=X+1
178 *enddo
179 *endif
180 *endif
181
182 *IF,K1,GT,2,THEN
183 *IF,G(X-1),GE,.2,THEN                !6th
184
185 EKILL,E1(K1)
186 K1=K1+1
187 K2=K2+1
188
189 ival=1
190 eval=40
191 *do,op,ival,eval
192 /solu
193 TIME,TM                              ! Time value
194 D,312, UZ, displacementy(TM), ,312
195 D,147, UZ, displacementy(TM), ,147
196
197 D,573, UZ, idisplacementy(TM), , 573
```

```
198 D,170, UZ, idisplacementy(TM), , 170
199
200
201 *IF,G(X-1),GE,.2,THEN                !6th
202 EKILL,E1(K1)
203 K1=K1+1
204 K2=K2+1
205
206 *elseif,G(X-1),LT,.2
207 *exit
208 *enddo
209 *endif
210 SOLVE                                 ! Initiate solution
calculations
211 finish
212
213 /post1
214 *GET,W2(X), node,NW2(K1), U,Z
215 *GET,resfd(X), node,312, U,Z
216
217 *GET,ff11(X), node,312, RF,FZ
218 *GET,ff12(X), node,147, RF,FZ  ! REACTION FORCE AT TIPS
219
220 *GET,ff15(X), node,573, RF,FZ
221 *GET,ff16(X), node,170, RF,FZ
222
223 *GET,resfd2(X), node,573, U,Z
224
225 a=ff11(x)+ff12(x)
226
227
228
229 resff2(X)=a
230
231 /post26
232 esol,2,E1(K1),NRFZ2(K1),F,Z,NF1
233 vget,RFz1(X),2,X               ! Store time history data
of variables
234
235 finish
236
237 G(X)=(-1*2*RFz1(x)*W2(X))/40
238 X=X+1
```

```
239 *enddo
240 *endif
241 *endif
242 SOLVE                                   ! Initiate solution
calculations
243
244 finish
245
246 /post1
247
248 *GET,W2(X), node,NW2(K1), U,Z
249
250
251
252
253
254 *GET,resfd(X), node,312, U,Z
255
256 *GET,ff11(X), node,312, RF,FZ
257 *GET,ff12(X), node,147, RF,FZ  ! REACTION FORCE AT TIPS
258
259 *GET,ff15(X), node,573, RF,FZ
260 *GET,ff16(X), node,170, RF,FZ
261
262 *GET,resfd2(X), node,573, U,Z
263
264 a=ff11(x)+ff12(x)
265
266
267
268 resff2(X)=a
269
270 finish
271
272 /post26
273 esol,2,E1(K1),NRFZ2(K1),F,Z,NF1
274 vget,RFz1(X),2,X                ! Store time history data
of variables
275
276 finish
277
278 G(X)=(-1*2*RFz1(x)*W2(X))/40
279
```

```
280
281
282
283
284 X=X+1
285
286 finish
287
288 *Enddo
289
290 *VPLOT,Resfd(1), Resff2(1)
291 *cfopen,UVTRUE2.txt
292 *CFCLOSE
293 PARSAV,ALL,'UVTRUE2','txt',' '
294 *CFCLOSE
295
296 !*CFOPEN,disp,dat
297 !*VWRITE,UX55(1) ! Write array in given format to file
"disp.dat"
298 !(6x,f12.6)
299 !*CFCLOSE
300 !finish
301 !*ENDDO
```

REFERENCES

1. Valisetty,R.R. and Rehfield,L.W., *A New Ply Model for Interlaminar Stress Analysis, Delamination and Debonding of Materials*, ASTM STP 876, W.S. Johnson (eds.), American Society for Testing and Materials, Philadelphia, pp 52-68, 1985.

2. N.J. Pagano, G.A. Schoeppner, *Delamination of polymer matrix composites: problems and assessment*, Kelly, A.; Zweben, D. (eds.), Oxford UK, 2000.

3. Turon Travesa A., *Simulation of Delamination in Composites Under Quasi-Static and Fatigue Loading Using Cohesive Zone Models*, PHD Thesis, University of Girona, 2006.

4. T.E. Tay, F. Shen, *Analysis of delamination growth in laminated composites with consideration for residual thermal stress effects*, Journal of Composite Materials, pp.1299-1320, 2002.

5. A.S. Crasto, R.Y. Kim, *Hygrothermal influence on the free-edge delamination of composites under compressive loading, In: Composite Materials*: Fatigue and Fracture 6, Armanios (eds.), E.A., Philadelphia, 1997.

6. V.V. Bolotin, *Delaminations in composite structures: Its origin, buckling, growth and stability*, Composites Part B-Engineering 27, pp. 29-145, 1996.

7. V.V. Bolotin, *Mechanics of delaminations in laminate composite structures*, Mechanics of Composite Materials 37 , pp. 367-380, 2001.

8. Reeder JR., *An evaluation of mixed-mode delamination failure criteria*, NASATM 104210, NASA Langley Research Center, 1992.

9. Emile S. Greenhalgh, Charlotte Rogers, Paul Robinson, *Fractographic observations on delamination growth and the subsequent migration through the laminate, Composites Science and Technology*, 2009.

10. Johannesson T, Sjoblom P, Selden R. *The detailed structure of delamination fracture surfaces in graphite/epoxy laminates*. J Mater Sci, pp.1171–1177, 1984.

11. Charalambides M, Kinloch AJ, Wang Y, Williams JG, *On the analysis of mixed mode failure*, Int J Fracture, pp.269–91, 1992.

12. W.L. Bradley, C.R. Corleto, D.P. Goetz, *Fracture physics of delamination of Composite materials*, AFOSR-TR-88-0020, 1987.

13. N. Blanco, Variable *mixed-mode delamination in composite laminates under fatigue conditons: testing and analysis*, PhD Thesis, University of Girona, 2005.

14. I.W. Obreimoff, *The splitting strength of mica*, Proceedings of the RoyalSociety of London A 127, pp. 290–297, 1930.

15. Paul Robinson, *Delamination Research: Progress in The Last Two Decades and The Challenges Ahead*, comptest'06, 2006.

16. Griffith, A. A, *The phenomena of rupture and flow in solids. Philosophical Transition*, Series A 221, pp.163-197, 1921.

17. Riveros, G. A., *Numerical Evaluation of Stress Intensity Factors (KI) J-Integral Approach*, Us Army Corps. of Engineering, 2007.

18. Irwing, G. R., *Analysis of stress and strain near the end of a crack traversing a plate*, Journal of Applied Mechanics ASME 24, pp.361-364, 1957.

19. Rice, J. R., *A path independent integral and the approximate analysis of strain concentrations by notches and cracks*, J. Appl. Mech. ASME 35, pp.379-386, 1968.

20. Rice, J. R., *Mathematical analysis in the mechanics of fracture. Fracture – An advance Treatise*, Vol. 2, ed., H. Liebowitz. New York: Academic Press, 1968.

21. Riveros, G. A., and Gopalaratnam, V. S. (in preparation). *Post-cracking behavior of reinforced concrete deep beams: A numerical fracture investigation of concrete strength and beam size*, ASCE Structural Journal.

22. Bazant, Z. P., and J. Planas, *Fracture and size effect in concrete and other quasibrittle materials*, Boca Raton (eds.), FL CRC Press, 1998.

23. T. L. Anderson. *Fracture Mechanics, Fundamentals and Applications*. CRC Press, Inc., Boca Raton (eds.), Florida, pp.36-41, 1991.

24. Z. Zou, S.R. Reid, S. Li, P.D. Soden, *Mode separation of energy release rate for delamination in composite laminates using sublaminates*, International Journal of Solids and Structures, pp. 2597-2613, 2001.

25. R. Krueger, *The virtual crack closure technique: history, approach and applications*, NASA/CR-2002-211628, 2002.

26. E.F. Rybicki, M.F. Kanninen, *A finite element calculation of stress intensity factors by a modified crack closure integral*, Engineering Fracture Mechanics, 9 , pp. 931-938, 1977.

27. Ortiz and Pandolfi, A., *Finite-deformation irreversible cohesive elements for three dimensional crack-propagation analysis*, International Journal for Numerical Methods in Engineering, pp. 1267-1282, 1999.

28. Kregting René, “Cohesive zone models towards a robust implementation of irrversible behavior” , pp. 2, 2005.

29. Chandra, N., Li, H., Shet, C. and Ghonem, H., *Some issues in the application of cohesive zone models for metal-ceramic interfaces*, International Journal of Solids and Structures, pp. 2827-2855, 2002.

30. L. M. Kachanov, *Introduction to continuum damage mechanics*, Martinus Nijhofi Publishers, Dordrecht, 1986.

31. Dávila, C. G. and E. R. Johnson, "Analysis of Delamination Initiation in Post buckled Dropped-Ply Laminates," AIAA Journal, Vol. 31, pp.721-727, 1993.

32. R. M. Jones, *Mechanics of Composite Materials*. Taylor and Francis, London, 2nd. Edition, 1999.

33. Jensen, H.M., Sheinman, I.,. *Straight-sided, buckling-driven delamination of thin films at high stress levels*, International Journal of Fracture, pp. 371-385, 2001.

34. Glaessgen, E.H., Raju, I.S., Poe, C.C., *Analytical and experimental studies of the debonding of stitched and unstitched composite joints*, Journal of Composite Materials, pp. 2599-2622, 2002.

35. Davies, P., *Round robin analysis of $G_{(Ic)}$ interlaminar fracture test*, Applied Composite Materials, pp. 135-140, 1996.

36. ASTM D 5528-01, *Standard test method for mode I interlaminar fracture toughness of unidirectional fibre-reinforced polymer matrix composites*, Annual Book of ASTM Standards, 15.03. Philadelphia (USA), 2003.

37. Whitney, J.M., Browning, C.E., Hoogstenden, W., *A double cantilever beam test for characterizing mode I delamination of composite materials*, Journal of Reinforced Plastics and Composites 1, pp. 297-313, 1982.

38. Nicholls, D.J., Gallagher, P.J., *Determination of GIc in angle ply composites using a cantilever beam test method*, Journal of Reinforced Plastics and Composites 2, 1983.

39. Robinson, P., Hodgkinson, J.M., *Interlaminar fracture toughness. Mechanical Testing of Advanced Fibre Composites*, Hodgkinson, J.M. (eds.), Woodhead Publishing, Cambridge (UK), pp. 170-210, 2000.

40. Tanaka, K., Tanaka, H., *Stress-ratio effect on mode II propagation of interlaminar fatigue cracks in graphite/epoxy composites. Composite Materials: Fatigue and Fracture 6*, ASTM STP 1285, Armanios (eds.), E.A. American Society for Testing and Materials, pp. 126-142, Philadelphia (USA), 1997.

41. Reeder, J.R., *An evaluation of mixed-mode delamination failure criteria*. NASATechnical Paper 104210, National Aeronautics and Space Agency, USA, 1992.

42. Reeder, J.R., *Refinements to the mixed-mode bending test for delamination toughness*, Journal of Composites Technology & Research 25 (4), pp. 191-195, 2003.

43. ASTM D 6671-01, *Standard test method of mixed mode I-mode II interlaminar fracture toughness of unidirectional fibre reinforced polymer matrix composites*, Annual Book of ASTM Standards, Philadelphia (USA), 2003.

44. Kinloch, A.J., Wang, Y., Williams, J.G., Yayla, P., *The mixed-mode delamination of fiber composite-materials*, Composites Science and Technology, pp. 225-237, 1993.

45. Greenhalgh, E., Singh, S., *Investigation of the failure mechanisms for delamination growth from embedded defects*, Proceedings of the 12th International Conference on Composite Materials, Paris (France), 1999.

46. Whitcomb, J.D., *Parametric analytical study of instability-related delamination growth*, Composites Science and Technology, pp. 19-48, 1986.

47. Wu, E.M., Reuter, R.C., *Crack extension in fibreglass reinforced plastics and a critical examination of the general fracture criterion*, Texas AM, USA, 1965.

48. Hutchinson, J.W., Suo, Z., *Mixed mode cracking in layered materials*, Advances in Applied Mechanics 29, Hutchinson, J.W., Wu, T.Y (eds.), Academic Press Inc., pp. 63-191, Boston (USA), 1992.

49. Benzeggagh, M.L., Kenane, M., *Measurement of mixed-mode delamination fracture toughness of unidirectional glass/epoxy composites with mixed-mode bending apparatus*, Composites Science and Technology, pp. 439-449, 1996.

50. K. He et al., *The study of tapered laminated composite structures: a review*, Composites Science and Technology, pp 2643-2657, 2000.

51. Hexply F584 Product Data, http://www.hexcel.com/Resources/DataSheets/Prepreg-Data-Sheets/F584_us.pdf

52. Donald F. Adams, Leif A. Carlsson, R. Byron Pipes, *Experimental Characterization of Advanced Composite Material*, 3rd edition , pp.64, CRC Press LLC, 2003.

53. M. Meo, E. Thieulot, *Delamination modelling in a double cantilever beam. Composite Structures*, pp. 429–434, 2005.

54. Andrzej Leski, *Implementation of the virtual crack closure technique in engineering FE calculations*, Finite Elements in Analysis and Designs , pp 261-268, 2007.

55. ISI Web of Knowledge, Published by Thomson Reuters.

56. G. Alfano, M. Crisfield, *Finite element interface models for the delamination analysis of laminated composites: mechanical and computational issues,International Journal for Numerical Methods in Engineering*, 77 (2), pp. 111-170, 2001.

57. ASTM D 5528-01, *Standard Test Method for Mode I Interlaminar Fracture Toughness of Unidirectional Fiber-Reinforced Polymer Matrix Composites*, 2007.

58. Simulia ABAQUS 6.9 Documentation.